

University of Leipzig
Faculty of Physics and Earth Sciences
Leipzig Institute for Meteorology

Characterization of aerosol properties by lidar measurements at Haifa, Israel

Master thesis

submitted by: Silke Mewes ()

Supervisor and contact person: Dr. Dietrich Althausen

Co-Supervisor: Prof. Dr. Manfred Wendisch

Leipzig, 17 July 2018

Abstract

The master thesis presents the vertical aerosol characterization at Haifa, Israel, which is based on 107 manually evaluated lidar profiles from March to September 2017. It should be found out which aerosol type occurred and if seasonal differences can be observed. Besides the lidar measurements with the Polly^{XT}, the models HYSPLIT and FLEXPART were used to determine the source of the aerosol particles. One case study is used to show that lidar measurements allow to examine the planetary boundary layer in detail and over a longer measuring period. In a second case study, the land sea breeze was investigated at this site. A third case study characterizes an aerosol layer consisting of dust from the Saharan desert. The major part of this study is dedicated to the monthly characterization of the atmospheric particles. This characterization revealed that the mainly detected aerosol type during the measuring period is a mixture of different aerosol types. In April and May, aerosol particles were transported over longer distances to Haifa because of the Sharav cyclone as well as rather low pressure system from west. These months can be seen as a dust season. In contrast to this, more urban aerosol particles originated from the surrounding area of Haifa were observed from June to August because of the subtropical high which caused stable weather conditions.

Contents

Abstract	3
1 Introduction	7
2 Data and methods	9
2.1 Scattering of light by particles	9
2.2 Lidar equations	10
2.2.1 Lidar equation (elastic backscattering)	10
2.2.2 Klett method	11
2.2.3 Raman method (inelastic backscattering)	12
2.3 Intensive and extensive quantities	14
2.3.1 Backscatter and extinction coefficient	14
2.3.2 Depolarization ratio	15
2.3.3 Lidar ratio	15
2.3.4 Ångström exponent	16
2.3.5 Poliphon calculation	16
2.4 Measuring system Polly ^{XT}	17
2.5 Auxiliary data	18
2.5.1 HYSPLIT trajectory model	18
2.5.2 FLEXPART model	19
2.5.3 Sun photometer	19
3 Aerosol	20
3.1 Aerosol types	20
3.1.1 Marine aerosol (sea salt)	20
3.1.2 Urban aerosol	20
3.1.3 Mineral dust	21
3.2 Criteria for aerosol type identification	22

4	Typical meteorological conditions in Haifa	23
4.1	Planetary boundary layer (PBL)	23
4.1.1	Types of PBL	23
4.1.2	Determination of the PBL height with lidar	25
4.2	Typical weather conditions at Israel	25
4.3	Land and sea breeze	27
5	Measurement examples	29
5.1	Development of the PBL on 4 April 2017	29
5.2	Record of land sea breeze	30
5.3	Aerosol layer on 9 June 2017	33
6	Classification of aerosol layers	37
7	Summary and discussion	53
	Literature	60

1 Introduction

On earth, there are various aerosol sources which are characteristic for the corresponding region. Dynamic processes in the Earth's atmosphere cause that, for example, Saharan dust is transported to the Caribbean or biomass burning aerosol from Siberia is transported eastwards over north America to Europe. Kubilay et al. (2000) studied the long-range transport of African dust to the eastern Mediterranean area and found that the dust concentration is higher in spring and autumn than in summer and winter. One reason for this observation is the Sharav cyclone where dust is carried from north Africa and Middle East. Similarly, Israelevich et al. (2003) describe an annual variation of desert dust over Israel. Because of the Sharav cyclone, desert aerosol is transported from sources in Chad to the eastern Mediterranean area in spring. In July and August, the aerosol particles are transported from sources near the Red Sea over Egypt to Israel. Additionally, Koçak et al. (2004) compile air flow sectors for the Israeli measurement site Haifa. Their measurements focus on the trace metal aerosol concentration for Haifa and show its seasonal variations and sources. The concentrations of aluminium, iron and manganese are higher during the transitional months (March, April, May and October) than during summer and winter. Koçak et al. (2004) recognized a greater frequency and intensity of dust events during this transitional months.

The lidar measurements (Light detection and ranging) at the Israeli coastal town Haifa are part of a three-year research project, which is funded by the German-Israeli Foundation for Scientific Research and Development. The Leibniz Institute for Tropospheric Research (TROPOS) Leipzig works together with the Technion - Israel Institute of Technology in Haifa. Wide-angle cameras are placed around the lidar to determine the aerosol distribution in the atmosphere. The aim of this study is to reconstruct the aerosol distribution with the cameras in a geometrical and complex form. Furthermore, it is possible to continuously record the vertical aerosol distribution above the measurement site with lidar over a longer period. So the development of the planetary boundary layer and the properties of the aerosol particles can be characterize.

Haifa is located in northern Israel at the coast of the Mediterranean Sea. Numerous industries and oil refineries are settled in the metropolitan region (Ganor et al., 1998).

Moreover, the orography of Haifa is characterized by some hills and mountains and the coastal line is not straight due to the Haifa Bay. The climate conditions can be assigned to the subtropical climate zone with hot and dry summer (W. Köppen climate classification) and with west coast winter rain climate (E. Neef climate classification) (Michael et al., 2002). Furthermore, there is a short distance to the Saharan desert and desert regions in the Middle East. Therefore, different aerosol types are expected to be present in this region. Until now, there is no systematic study about the vertical aerosol distribution above Haifa. There are Israeli measuring sites which are located in the south (Jerusalem, Beer Sheba) where more influence of the desert is apparent. Also lidar measurements are rare in the Middle East. Therefore, a new lidar site in Haifa is an enrichment for the aerosol research in the eastern Mediterranean area. Further comparable lidar measurements at other measuring sites can be found in the network "PollyNET" (Baars et al., 2016).

The aim of this thesis is the aerosol characterization at Haifa. Based on 107 manually evaluated lidar profiles from the measuring period from March to September 2017. Three case studies are discussed. First, the development of the boundary layer is presented which is measured continuously by the lidar. The different types of the planetary boundary layer from Stull (1988) are characterized as well. Because of the location of the measurement site at the coast of the Mediterranean Sea, the question arises, if and how much the land sea breeze influences the vertical aerosol distribution besides the daily development of the boundary layer. Ganor et al. (1998) have already examined aerosol samples during land sea breeze in Haifa Bay. They identified local aerosol during land breeze which is characterized by phosphate, fly ash and soil particles. The second case where the land sea breeze is investigated using lidar measurements describes the differences in transported aerosol during land sea breeze that had be detected. The last case examines a dust event that occurred on 9 June 2017. The dust source and the dust transport is investigated.

In the second part of the thesis, the vertical distribution of different aerosol types is shown on a monthly basis to study possible seasonal differences of the layers. These layers are characterized by using the method from Baars et al. (2017). Furthermore, it will be explained how the heights of the detected aerosol layers are determined.

In Chapter 2, the theoretical basics for the lidar measurements are explained as well as the used measuring instruments and trajectory models are described. In Chapter 3, the expected aerosol types are described and the aerosol classification is presented. In Chapter 4, the meteorological conditions that influence the aerosol distribution are presented. Three case studies follow in Chapter 5. Chapter 6 describes the aerosol classification which is applied to all evaluated lidar profiles from March to September 2017 and the vertical distributions of the detected aerosol layers. Finally, a summary with an outlook on possible future work is given.

2 Data and methods

The theoretical basics of the aerosol lidar technique are illustrated in this chapter. First, the light scattering by particles is described and the lidar equations for determining the target quantities are presented. The intensive and extensive quantities, which are necessary for characterizing aerosol types, are explained in the third section. At the end, the measuring system Polly^{XT} and auxiliary data are described.

2.1 Scattering of light by particles

Bohren and Huffman (1983) describe an obstacle (e.g., single electron, atom, molecule, solid or liquid particle) which is illuminated by an electromagnetic wave. The electric charges in the obstacle are set into oscillatory motion due to the electric field of the incident electromagnetic wave and the obstacles radiate electromagnetic energy in all directions. So the obstacle scatters this radiation and Bohren and Huffman (1983) define this scattering as the sum of excitation and reradiation of objects after initiation. The angular distribution is described by the scattering function of the scattered electromagnetic wave. Furthermore, absorption is defined as transformation of parts of the incident electromagnetic energy into other forms (e.g., thermal energy).

Bohren and Huffman (1983) mention that the scattering function of the particle and the amount of absorbed light depend on particle properties (shape, size and composition). According to Demtröder (2009), Rayleigh scattering is light scattering at atoms and molecules with an average diameter much smaller than the wavelength λ . Characteristic scatterers are air molecules and aerosol particles smaller than 0.1 μm in diameter (Roedel and Wagner, 2011) and the backscatter coefficient is proportional to $1/\lambda^4$ (Klein and Werner, 1993).

Scatterers like aerosol particles, haze, cloud droplets, which are larger or equal in diameter than the wavelength of the incident light, show a different behaviour and are described by the Mie theory (Mie, 1908; Roedel and Wagner, 2011).

2.2 Lidar equations

The lidar technique is based on scattering processes of photons from laser light pulses by atmospheric particles and molecules (Weitkamp, 2006). After the scattering event, the backscattered light is recorded with time. The distance Z between the lidar system and the scattering volume results from the detection time t after the emission of the respective laser pulse and the speed of light c : $Z = \frac{ct}{2}$.

The lidar equations are formulated for elastic and inelastic backscattering. There is no energy change of photons in case of the elastic scattering, but an energy change of photons appears during the inelastic scattering.

2.2.1 Lidar equation (elastic backscattering)

The target quantities (i.e., particle extinction coefficient α_{par} , particle backscatter coefficient β_{par} , the volume and particle linear depolarization ratio δ^{vol} , δ^{par}) can be determined from the received power $P(Z, \lambda)$ measured by the lidar (Weitkamp, 2006):

$$P(Z, \lambda) = \frac{KO(Z)}{Z^2} [\beta_{\lambda}^{par}(Z) + \beta_{\lambda}^{mol}(Z)] \exp \left(-2 \int_0^Z [\alpha_{\lambda}^{par}(z) + \alpha_{\lambda}^{mol}(z)] dz \right). \quad (2.2.1)$$

This equation can be separated into three parts: the system and geometry factor, backscatter term and transmission term. The system and geometry factor is defined as:

$$\frac{KO(Z)}{Z^2} \quad \text{with } K = P_0 \frac{c\tau}{2} A\eta. \quad (2.2.2)$$

The system factor K contains the original power P_0 of the emitted laser pulse, its temporal pulse length τ , the area of the receiving optic A and the system efficiency η . The overlap function $O(Z)$ characterizes the overlap between the outgoing laser beam and the receiver field of view.

The backscatter term is divided into a particle and a molecular backscatter coefficient. It is a measure for the part of the emitted laser pulse which is backscattered to the lidar by the scatterers at the distance Z (Weitkamp, 2006).

The last term of eq. 2.2.1 characterizes the transmission and is derived from the Lambert-Beer-Bouguer law. The integral describes which part of the emitted power gets “lost“ on its way from lidar to a distance Z . A factor of 2 is applied because the laser beam passes the distance from laser to scattering volume and backwards (Weitkamp, 2006).

In this equation, the particle backscatter coefficient and the particle extinction coefficient are unknown quantities because the molecular contribution can be estimated well. Two possibilities to solve the lidar equation are described in the following sections.

2.2.2 Klett method

The Klett method (Klett, 1981; Fernald, 1984) has been developed to solve the elastic lidar equation where the overlap function $O(Z)$ is assumed to be 1. So it is valid for $Z_{overlap} < Z$. The range-corrected signal $S_{corr}(Z)$ is obtained by multiplication of $P(Z)$ by Z^2 . Applying the logarithm to both sides results in $S(Z) \equiv \ln[Z^2 P(Z)]$.

Klett (1981) changes the lidar equation (eq. 2.2.1) with $S = S(Z)$ and $S_0 = S(Z_0)$ where Z_0 is an assumed reference height to:

$$S - S_0 = \ln \frac{\beta}{\beta_0} - 2 \int_{Z_0}^Z \alpha dz. \quad (2.2.3)$$

Differentiation of this equation yields to:

$$\frac{dS(\lambda, Z)}{dZ} = \frac{1}{\beta(\lambda, Z)} \frac{d\beta(\lambda, Z)}{dZ} - 2\alpha(\lambda, Z). \quad (2.2.4)$$

The solution of the differential equation requires a known ratio of α_{par} to β_{par} : the lidar ratio (LR). The relation $\alpha = \alpha_{par} + \alpha_{mol} = LR(\beta_{par} - \beta_{mol}) + \alpha_{mol}$ is valid and changes the extinction coefficient in eq. 2.2.4:

$$\frac{dS}{dZ} = \frac{1}{\beta_{par}} \frac{d\beta_{par}}{dZ} - 2LR\beta_{par} + 2LR\beta_{mol} - 2\alpha_{mol}. \quad (2.2.5)$$

This non linear differential equation has the structure of a Bernoulli or homogeneous Ricatti equation. Transformation of the equation leads to:

$$\frac{d\beta_{par}}{dZ} - 2LR\beta_{par}^2 - \left(\frac{dS}{dZ} + 2\alpha_{mol} + 2LR\beta_{mol} \right) \beta_{par} = 0. \quad (2.2.6)$$

Klett (1981) established the following relation for the backscatter coefficient with the condition $Z > Z_0$ (Z_0 is the lowest boundary of backscattering profile):

$$\beta_{par} = \frac{\exp(2\alpha_{mol} - 2LR\beta_{mol}Z + S(Z) - S(Z_0))}{\frac{1}{\beta_{par}(Z_0)} - 2LR \int_{Z_0}^Z \exp(2z'(\alpha_{mol} - LR\beta_{mol}) + S(z') - S(z'_0)) dz'}. \quad (2.2.7)$$

But he recognized that a numerical stable solution cannot always be found for this analytic correct solution, so he modified the integration limits in the denominator. The sign changes to:

$$\beta_{par} = \frac{\exp(2\alpha_{mol} - 2LR\beta_{mol}Z + S(Z) - S(Z_0))}{\frac{1}{\beta_{par}(Z_{ref})} + 2LR \int_Z^{Z_{ref}} \exp(2z'(\alpha_{mol} - LR\beta_{mol}) + S(z') - S(z'_0)) dz'}. \quad (2.2.8)$$

It is important to choose a range for $Z < Z_{ref}$ and a reference height where no particles are present and thus only Rayleigh scattering occurs, so that a very small reference value can be estimated. The vertical profile of the particle extinction coefficient can be calculated by $\alpha_{par}(Z) = LR(Z)\beta_{par}(Z)$ on this basis (Weitkamp, 2006). So the lidar ratio can be calculated with:

$$LR(Z) = \frac{\alpha_{par}(Z)}{\beta_{par}(Z)}. \quad (2.2.9)$$

In accordance to Müller et al. (2003), the Klett method contains more errors than the following Raman method because of the assumed constant lidar ratio. There are very large uncertainties related to this assumption as it was shown in Sasano et al. (1985), too.

2.2.3 Raman method (inelastic backscattering)

The elastic signals at 355 and 532 nm wavelength and the inelastic signals at 387 and 607 nm wavelength from Raman scattering of nitrogen molecules are used for the Raman method. Signal ratios between the elastic and inelastic Raman signal are used to calculate the backscatter coefficients (355, 532 nm) (Ansmann et al., 1992b).

The Raman signal $P(Z, \lambda_{Ra})$ is measured at the Raman wavelength λ_{Ra} . The signal represents the backscattering of the atmospheric volume at the distance Z and is described by the Raman lidar equation (Weitkamp, 2006):

$$P(Z, \lambda_{Ra}) = \frac{P_0 \eta_{\lambda_{Ra}}}{Z^2} O(Z, \lambda_{Ra}) \beta_{Ra}(Z, \lambda_0) \exp\left(-\int_0^Z (\alpha(z, \lambda_0) + \alpha(z, \lambda_{Ra})) dz\right). \quad (2.2.10)$$

where $\alpha(Z, \lambda_0)$ is the range-dependent extinction at locations between lidar and backscattering volume at the wavelength λ_0 and $\alpha(Z, \lambda_{Ra})$ is the range-dependent extinction at locations between backscattering volume and lidar at the wavelength λ_{Ra} which causes the attenuation of the signal strength. $\lambda_{Ra} = \lambda_0$ can be used for the rotational Raman case.

The molecular backscatter coefficient is calculated from the density of molecules. N_{Ra} is

the number density of nitrogen and oxygen and $d\sigma_{Ra}/d\Omega(\pi, \lambda_0)$ is the differential scattering cross section for the Raman scattering at laser wavelength λ_0 and the scattering angle π :

$$\beta_{Ra}(Z, \lambda_0) = N_{Ra}(Z) \frac{d\sigma_{Ra}}{d\Omega}(\pi, \lambda_0). \quad (2.2.11)$$

Eq. 2.2.11 is inserted in eq. 2.2.10 and the logarithm of both sides of the resulting equation is taken. After that, differentiation of the equation with respect to Z and rearranging leads to the total extinction coefficient. Hereby, the range-corrected signal is $S_{corr,Ra}(Z, \lambda_{Ra}) = Z^2 P(Z, \lambda_{Ra})$ (Weitkamp, 2006):

$$\alpha(Z, \lambda_0) + \alpha(Z, \lambda_{Ra}) = \frac{d}{dZ} \ln \frac{N_{Ra}(Z)}{S_{corr,Ra}(Z, \lambda_{Ra})} + \frac{d}{dZ} \ln O(Z, \lambda_{Ra}). \quad (2.2.12)$$

The overlap is 1 for large distances. Hence, the overlap term in eq. 2.2.12 can be ignored and the equation is written with the definition of the extinction coefficient ($\alpha(Z) = \alpha_{par}(Z) + \alpha_{mol}(Z)$):

$$\alpha_{par}(Z, \lambda_0) + \alpha_{par}(Z, \lambda_{Ra}) = \frac{d}{dZ} \ln \frac{N_{Ra}(Z)}{S_{corr,Ra}(Z, \lambda_{Ra})} - \alpha_{mol}(Z, \lambda_0) - \alpha_{mol}(Z, \lambda_{Ra}). \quad (2.2.13)$$

The Ångström exponent $\mathring{A}(Z)$ describes the wavelength dependence of the extinction: $\alpha_{par}(\lambda_0)/\alpha_{par}(\lambda_{Ra}) = (\lambda_{Ra}/\lambda_0)^{\mathring{A}}$. Taking \mathring{A} into account, the extinction coefficient at the transmitted wavelength is obtained (Weitkamp, 2006):

$$\alpha_{par}(Z, \lambda_0) = \frac{\frac{d}{dZ} \ln \left(\frac{N_{Ra}(Z)}{S_{corr,Ra}(Z, \lambda_{Ra})} \right) - \alpha_{mol}(Z, \lambda_0) - \alpha_{mol}(Z, \lambda_{Ra})}{1 + \left(\frac{\lambda_0}{\lambda_{Ra}} \right)^{\mathring{A}}}. \quad (2.2.14)$$

The particle backscatter coefficient $\beta_{par}(Z, \lambda_0)$ can be determined from the particle extinction coefficient $\alpha_{par}(Z, \lambda_0)$ by using the lidar signals $P(Z, \lambda_0)$ (cf. eq. 2.2.1) and $P(Z, \lambda_{Ra})$ (cf. eq. 2.2.10) for (Weitkamp, 2006):

$$\begin{aligned} \beta_{par}(Z, \lambda_0) + \beta_{mol}(Z, \lambda_0) &= [\beta_{par}(Z_0, \lambda_0) + \beta_{mol}(Z_0, \lambda_0)] \times \frac{P(Z_0, \lambda_{Ra})P(Z, \lambda_0)}{P(Z_0, \lambda_0)P(Z, \lambda_{Ra})} \frac{N_{Ra}(Z)}{N_{Ra}(Z_0)} \\ &\times \frac{\exp \left(- \int_{Z_0}^Z [\alpha_{par}(z, \lambda_{Ra}) + \alpha_{mol}(z, \lambda_{Ra})] dz \right)}{\exp \left(- \int_{Z_0}^Z [\alpha_{par}(z, \lambda_0) + \alpha_{mol}(z, \lambda_0)] dz \right)}. \end{aligned} \quad (2.2.15)$$

The lidar ratio can be calculated with the Raman method where two equations have used to determine the two unknown quantities α_{par} and β_{par} with eq. 2.2.9.

During daytime, the measurements with the Raman method are difficult because the scattering efficiency is smaller by a factor of 10^{-3} than the efficiency of the elastic backscattering. Thus, the detectors of the lidar have to be adjusted very sensitively. Because of the low signal intensity compared to the high background radiation of the daylight, the Raman method is mainly applied during night measurements.

2.3 Intensive and extensive quantities

The two extensive quantities backscatter and extinction coefficient depend on the amount of the scattering particles. The intensive quantities, depolarization ratio, lidar ratio and Ångström exponent do not depend on the mass (or amount of scattering particles), but they depend on the type, shape and size of the particles and are described in the Sections 2.3.2 to 2.3.4.

2.3.1 Backscatter and extinction coefficient

The strength of the lidar signal is intrinsically determined by the backscatter coefficient $\beta(R, \lambda)$. It describes how much light is scattered into the backward direction, towards the lidar receiver, and can be written as sum over all scatterers (molecules and particles). It is a specific value of the scattering coefficient for the scattering angle $\theta = 180^\circ$. In the case studies (Chapter 5), the uncalibrated attenuated backscatter coefficient is applied. It is like the range-corrected signal to get a qualitative view about the development of the layering.

The extinction coefficient $\alpha(R, \lambda)$ is defined as the product of the number concentration and the extinction cross section for each type of scatterer. So scattering and absorption of light by molecules and particles causes extinction.

Ansmann et al. (1992a) estimate the Raman lidar measurement uncertainties of the backscatter coefficient and the extinction coefficient to be in the range of 5% to 10% and 10% to 20%, respectively.

2.3.2 Depolarization ratio

The extensive quantity volume linear depolarization ratio δ^{vol} defines the ratio of the total cross- to the total parallel-polarized backscatter coefficient (Freudenthaler et al., 2009):

$$\delta^{vol}(Z) = \frac{\beta_{\perp}}{\beta_{\parallel}} = \frac{P_{\perp}}{P_{\parallel}}. \quad (2.3.1)$$

The particle linear depolarization ratio can be calculated from the volume linear depolarization ratio. It is the ratio of particle backscattering coefficients in the perpendicular to the parallel polarization plane and can be determined as (Freudenthaler et al., 2009):

$$\delta^{par}(Z) = \frac{\beta_{\perp}^{par}}{\beta_{\parallel}^{par}} = \frac{(1 + \delta^{mol})\delta^{vol}\left(\frac{\beta^{mol} + \beta^{par}}{\beta^{mol}}\right) - (1 + \delta^{vol})\delta^{mol}}{(1 + \delta^{mol})\left(\frac{\beta^{mol} + \beta^{par}}{\beta^{mol}}\right) - (1 + \delta^{vol})}. \quad (2.3.2)$$

Thereby, δ^{mol} is the linear depolarization ratio of air molecules ($\delta^{mol} = \beta_{\perp}^{mol}/\beta_{\parallel}^{mol}$). The linear particle depolarization ratio is about zero for spherical particles and larger than zero for a non-spherical shape. Thus, statements about the relevant particle type can be made. The lidar measurement uncertainties of the linear depolarization ratio (355, 532 nm) are between 7% to 14% and caused by the uncertainties of the particle backscatter coefficient (Hofer et al., 2017).

2.3.3 Lidar ratio

The lidar ratio (LR) is the ratio of extinction to backscatter coefficient (Ansmann et al., 1992b) and can be calculated with eq. 2.2.9.

The lidar ratio is a parameter for the determination of the particle type. For the Klett method, the value of the LR is assumed to be constant, so it is not a measured value. With the Raman method, the lidar ratios at wavelengths of 355 and 532 nm are calculated from the extinction and backscatter coefficients at their respective wavelengths (Müller et al., 2003). The unit of the lidar ratio is steradian (sr). The lidar measurement uncertainties of the extinction and backscatter profiles lead to a relative error of the lidar ratio which is between 11 and 22% (Hofer et al., 2017).

2.3.4 Ångström exponent

The Ångström exponent describes the wavelength dependence of the particle extinction coefficient or the particle backscatter coefficient and can be calculated from (Ångström, 1906):

$$\frac{\alpha(\lambda_1)}{\alpha(\lambda_2)} = \left(\frac{\lambda_2}{\lambda_1}\right)^{\mathring{A}(Z)} \quad \text{and} \quad \mathring{A}(R) = \frac{\ln\left(\frac{\alpha(\lambda_1)}{\alpha(\lambda_2)}\right)}{\ln\left(\frac{\lambda_2}{\lambda_1}\right)}. \quad (2.3.3)$$

In contrast to this, the backscatter related Ångström exponent is calculated from the particle backscatter coefficient at its respective wavelength (Giannakaki et al., 2010). The use of Ångström exponents at different wavelength ranges is of advantage, if the particle size distribution consists of fine particles (particle radius $\leq 0.5 \mu\text{m}$) and of particles with a radius $\geq 0.5 \mu\text{m}$ (Müller et al., 2003). For example, a value of 1 and higher indicates small particles, low values of e.g., 0.2 are measured for mineral dust (Baars et al., 2016). The lidar measurement uncertainties are caused by the relative error of individual backscatter profiles for the calculated backscatter Ångström exponent (7-14%) and the individual extinction profiles for the calculated extinction Ångström exponent (14-28%) (Hofer et al., 2017).

2.3.5 Poliphon calculation

The polarization lidar photometer networking (Poliphon) method is a technique for detailed vertical profiling of optical and micro physical properties of atmospheric particles (Ansmann et al., 2012). Mamouri and Ansmann (2014) describe the one-step Poliphon method and the extended Poliphon formalism which can separate non-dust and dust aerosol properties. Furthermore, their two-step Poliphon method divides fine-mode and coarse-mode dust properties. Ansmann et al. (2012) use the depolarization ratio to identify layers with non-spherical particles and to quantify their contribution to the lidar-derived profile of the particle backscatter coefficient. According to Ansmann et al. (2011), the uncertainties in the calculated mass concentration are between 30 and 50%.

The individual uncertainties of the extensive and intensive quantities are shown in Table 2.1. The largest values are used for calculating the maximum error of the measurements in Chapter 5.

Table 2.1: Products of the lidar Polly^{XT} and their relative uncertainties based on Hofer et al. (2017).

Quantity	Wavelength [nm]	Uncertainty [%]
β	355, 532, 1064	10
α	355, 532	20
LR	355, 532	22
δ	355, 532	14
\AA	bsc 355/532, bsc 532/1064	14
\AA	ext 355/532, ext 355/532 NF	28
mass conc.	from δ , β , 532	50

2.4 Measuring system Polly^{XT}

In Haifa, the Polly of the first generation (Polly^{1v2}) performed automatic lidar measurements between July 2016 and March 2017. A Polly^{XT} is measuring since March 2017. Polly^{XT} is an acronym for POrtabLe Lidar sYstem with eXTended capabilities (Engelmann et al., 2016) and is built in-house at the Leibniz Institute for Tropospheric Research. The instrument (Fig. 2.1a) is installed on the roof of Technion in Haifa. Figure 2.1b shows the Polly^{XT} at its measuring location with open doors to demonstrate its components. The Polly systems are usually housed in outdoor cabinets to allow measurements under the various climatic conditions. The autonomously running systems can be controlled by remote access. Measurements will be automatically interrupted and resumed thereafter, if rain events occur. Furthermore, modified ship radars are used to shut down the laser beam in case a plane is detected.

The Polly^{XT} emits linear polarized laser light with an energy of 180 mJ (at 1064 nm), 110 mJ (at 532 nm) and 60 mJ (at 355 nm) and runs in 24/7 mode. Based on Baars et al. (2016), this lidar system is a so-called 3+2+2+1+2+2 Raman, polarization and water-vapor lidar with near-range capabilities which means 3 elastic, 2 Raman, 2 depolarization, 1 water-vapor, 2 near-range elastic and 2 near-range Raman signals. Profiles of water vapor mixing ratio can be calculated from the 407 nm channel (Dai et al., 2018).

The latest system developments include a near-range receiver unit for elastic and Raman measurements of backscatter and extinction coefficient down to 120 m above ground, a water-vapor channel and the channels for simultaneous measurements of the particle linear depolarization ratio at 355 and 532 nm (Engelmann et al., 2016).

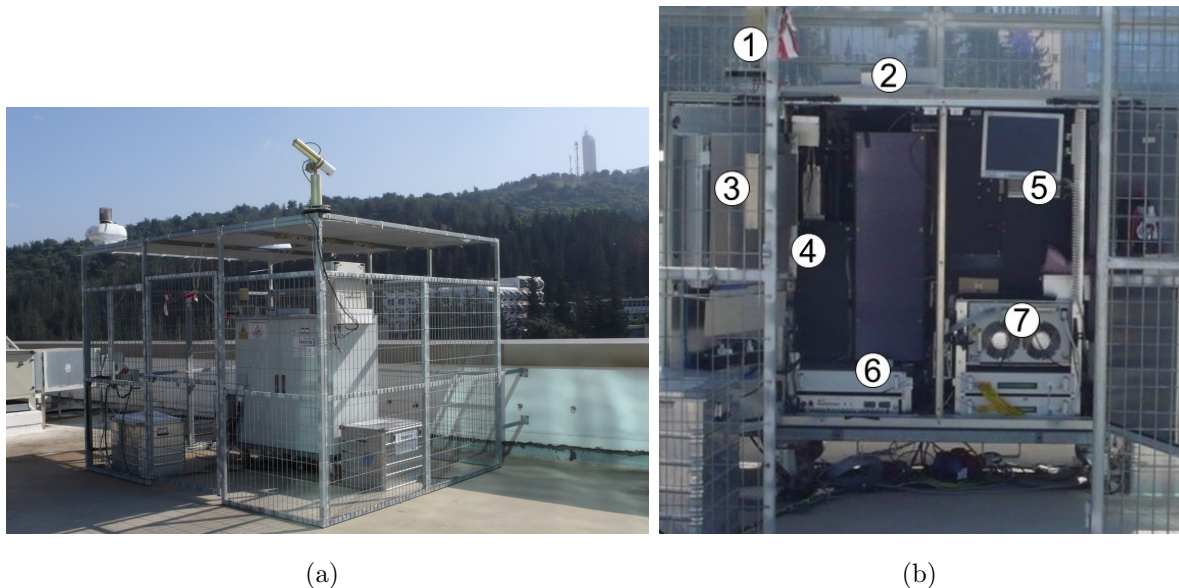


Figure 2.1: (a) Polly^{XT} on the roof of Technion in Haifa; (b) Open system showing major parts of Polly^{XT}: sensors for outdoor temperature and rain (1), roof cover (2), air conditioner (3), laser head and optical system (4), receiver with 8 channels (5), drawer with 4 sensors for the near-range channels (6), laser power supply (7); based on Althausen et al. (2009) and Engelmann et al. (2016).

2.5 Auxiliary data

2.5.1 HYSPLIT trajectory model

The Hybrid Single-Particle Lagrangian Integrated Trajectory model (HYSPLIT) computes air parcel trajectories, complex transport, dispersion, chemical transformation and deposition and is described in detail by Stein et al. (2015) and Rolph et al. (2017). Back-trajectory calculations, which are also used in Sect. 5.3, help to determine the possible particle loading areas of the observed air masses and describe the atmospheric transport, dispersion, and deposition of pollutants and hazardous materials.

2.5.2 FLEXPART model

The FLEXible PARTicle dispersion model (FLEXPART) is a Lagrangian transport and dispersion model and was designed for calculating long-range and mesoscale dispersion of air pollutants from point sources (Stohl et al., 2005). The Lagrangian particle model computes trajectories of a large number of infinitesimally small air parcels for describing transport and diffusion of tracers in the atmosphere (Stohl et al., 2005). This model can simulate the dispersion of tracers from their source forward in time or backward in time to determine the source contribution. Different versions of FLEXPART are based on meteorological data from ECMWF, GFS or from mesoscale models (Flexpart, 2018). The logarithm of the accumulated residence time is calculated and used in the case study (Sect. 5.3).

2.5.3 Sun photometer

The automatic-tracking sun and sky scanning radiometer performs direct sun measurements at the wavelengths 340, 380, 440, 500, 675, 870, 940 and 1020 nm every 15 min. The direct sun measurements with a 1.2° full field of view take 8 s due to a motor-driven filter wheel which places each filter in front of the detector. According to Holben et al. (1998), the sky measurements are made at the wavelengths 440, 670, 870 and 1020 nm. One basic sky observation sequence, which is called "almucantar", is a series of measurements which are taken at the sun elevation angle for specified azimuth angles relative to the position of the sun (360 degrees around). The other basic sky observation sequence is named as "principal plane" where it is measured in sun direction upwards in 180 degrees. The sun/sky radiometers are part of the AERONET (Aerosol Robotic Network) global network (Holben et al., 2001).

In general, this method is based on measurements of the spectral extinction of direct beam radiation by a filtered detector according to the Beer-Lambert-Bouguer law.

For the manually analyzed lidar profiles, the aerosol optical depth (AOD) is compared with the calculated AOD from lidar. This ensures that uncertainties in calculating the profiles for the intensive and extensive quantities are minimized.

3 Aerosol

3.1 Aerosol types

This chapter describes the three important aerosol types, marine aerosol, urban aerosol and mineral dust, that mainly occur in the surrounding area of Haifa. Especially mineral dust is often transported to the eastern Mediterranean region from sources in the Saharan desert and deserts in the Middle East. Marine aerosol occurs because of Haifa's location at the Mediterranean Sea. Furthermore, urban aerosol from the metropolitan area of Haifa is expected.

3.1.1 Marine aerosol (sea salt)

Haifa is a coastal town in the eastern Mediterranean area. Therefore, marine aerosol is assumed to be frequently present in the planetary boundary layer and in the free troposphere. Marine particles have a radius of about 0.01 to 100 μm which consist of sea salt (Groß, 2011). Moreover, the particles have a spherical shape in the marine boundary layer because of the high relative humidity (often greater than 80%) (Charlson and Heintzenberg, 1995). According to Haarig et al. (2017), the spherical sea salt particles become cubic-like when the relative humidity decreases below 45% and their optical properties (lidar ratio, depolarization ratio, backscatter and extinction coefficient) change.

This aerosol type shows characteristic values for the respective intensive quantities. For example, the lidar ratio is around 20 sr and the particle depolarization ratio is very low with less than 3% at 532 nm wavelength (Groß et al., 2013).

3.1.2 Urban aerosol

The source of urban aerosol is the metropolitan area of Haifa because numerous electrical and chemical industries as well as oil refineries are settled in the city and in the surround-

ing area (Ganor et al., 1998).

This aerosol type is especially abundant in the lower part of the troposphere (Charlson and Heintzenberg, 1995). On the one hand, the particles are emitted directly into the atmosphere (primary aerosols) and on the other hand, they can be formed by chemical reactions in the atmosphere (secondary aerosol) (Hallquist et al., 2009). The chemical components of urban aerosol vary depending on the emission sources and mainly contain sulphate, nitrate, organic components and graphite (Charlson and Heintzenberg, 1995). Seinfeld and Pandis (1998) characterize that urban aerosol particles are smaller than 0.1 μm in diameter and that the size distribution is being quite variable in urban areas. They describe that extremely high concentration of fine particles ($\leq 0.1 \mu\text{m}$) are close to the sources, but their concentration decreases rapidly with distance from the sources.

A lidar ratio of 80 sr is a typical value for urban aerosol and the particle depolarization ratio is smaller than 5% at 532 nm wavelength (Groß et al., 2013; Baars et al., 2016).

3.1.3 Mineral dust

Dust particles have a large range of size (0.01 to 100 μm) and a strongly irregular shape (Groß, 2011). Particles smaller than 10 μm are transported over long distances by the wind, while particles as large as 100 μm diameter were only found in the source regions (Seinfeld and Pandis, 1998).

Moreover, Charlson and Heintzenberg (1995) describe that dust particles influence the regional equilibrium of terrestrial radiation. The mineral particles contain iron oxide and cause absorption lines in the ultraviolet and near infrared range.

Two main emission sources are important for Haifa and the eastern Mediterranean area: on the one hand the Saharan desert and on the other hand the deserts in the Middle East (Syria, Saudi Arabia etc.). Israelevich et al. (2003) found out that the dust pollution is governed by seasonal variations. The desert aerosol from sources in Chad (Saharan desert) is transported to the eastern Mediterranean area in spring along the coast of North Africa. In July and August, mineral dust comes via Egypt from sources near the Red Sea. In autumn, the dust particles from the Libyan coast arrive at Israeli sites.

It has been found that the lidar ratio at 532 nm wavelength is 55 sr (Tesche et al., 2009) for pure Saharan dust and around 40 sr for Arabian dust (Nisantzi et al., 2015). The particle depolarization ratio is around 30% at 532 nm wavelength and lower, if the particle distribution is mixed or aged Saharan dust (Groß et al., 2013). Mamouri et al. (2013) determined particle depolarization ratios between 28 and 35% at 532 nm for Arabian dust.

3.2 Criteria for aerosol type identification

Baars et al. (2017) have developed a target classification with four aerosol and several cloud classes. The particles are classified by their shapes and sizes which are determined by the measured optical properties, instead of their sources. The cloud characterization is not considered in this thesis because only measurements in cloud-free cases are regarded. The received signals of the backscattered light at 532 and 1064 nm and the particle depolarization ratio at 532 nm are used as well as the Ångström exponent, calculated with the particle backscatter coefficients at 532 nm and 1064 nm wavelength. The thresholds of the criteria are obtained from multi-year, multi-site EARLINET (European Aerosol Research lidar Network) measurements and are listed in Table 3.1.

Table 3.1: Aerosol type criteria based on the measured linear particle depolarization ratio and Ångström exponent (Baars et al., 2017).

Aerosol types	δ_{par}^{532}	$\hat{A}_{532-1064}$
small (SML)	< 0.07	≥ 0.75
large, spherical (LAS)	< 0.07	< 0.75
mixture, partly non-spherical (MIX)	$0.07 \leq \dots < 0.20$	-
large, non-spherical (LNS)	$0.20 \leq \dots < 0.35$	-
not definable (n.d.)	-	-

The category "not definable" is added to the categorization because of the occurrence of unreliable data in the lowest and upper parts of the profiles. Based on the criteria and the known micro-physical properties, it is possible to associate urban aerosol with small aerosol and mineral dust may refer to large, non-spherical aerosol. Also marine aerosol allocates to the large, spherical aerosol type. Furthermore, the aerosol-mix with a large size range may consist of different mixture of these three aerosol types. The advantage of this characterization is that no values get lost within these considerations. This categorization was applied to case studies with clouds by Baars et al. (2017). For the first time in Haifa, this categorization was only applied to cloud-free cases during the measuring period.

The application of these classification are shown in one case study (Sect. 5.3) and the statistical analysis for the months March to September 2017 are presented in Chapter 6.

4 Typical meteorological conditions in Haifa

4.1 Planetary boundary layer (PBL)

The complete theoretical description of this section is based on Stull (1988).

He defines the boundary layer as the part of the troposphere which is directly influenced by the earth's surface and responds to surface forces with a time scale of about an hour or less. These forces are frictional drag, evaporation, transpiration, heat transfer and pollutant emission. Besides the boundary layer, the free atmosphere which is located between boundary layer and tropopause is characterized as the other part of the troposphere.

The thickness of the planetary boundary layer (PBL) is variable in time and space. There is also a diurnal variation of temperature near the earth's surface. Additionally, turbulence is the most important transport process besides mean wind and waves. Much of the PBL turbulence is generated by forces from the ground, for example, solar heating during sunny days or frictional drag on the air over ground.

4.1.1 Types of PBL

In low pressure regions, the convection can carry boundary layer air away from the ground to large altitudes of the troposphere. Therefore, it is difficult to determine a boundary layer top at low pressure conditions. In contrast, there is an easily defined PBL structure with a diurnal cycle over land surface in high pressure systems. In Fig. 4.1 the major components of the PBL are illustrated: the mixed layer, the residual layer and the stable boundary layer.

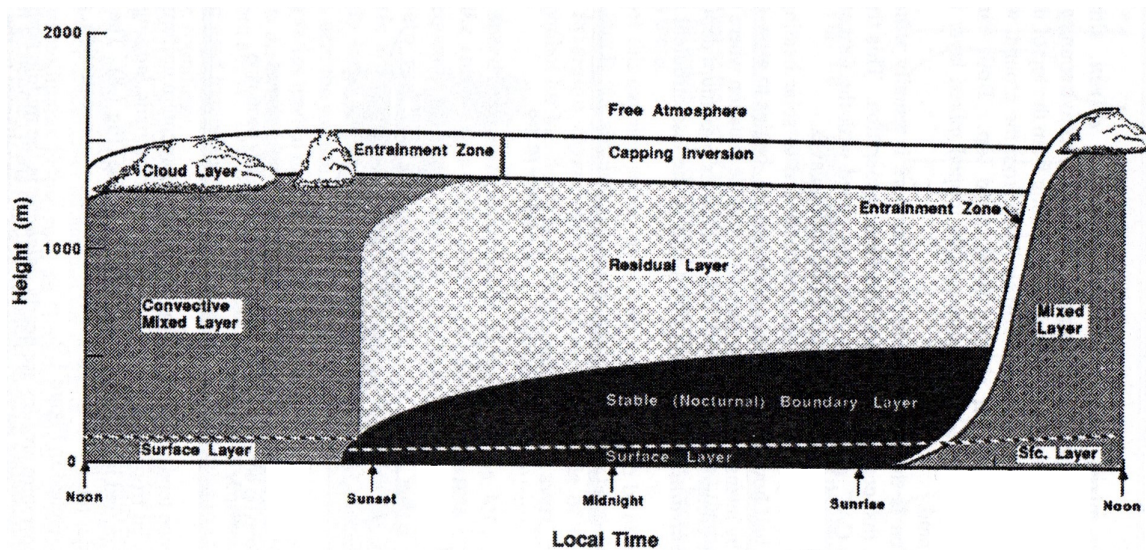


Figure 4.1: Vertical scheme of the PBL over land in high pressure regions. PBL consists of a very turbulent mixed layer, a less-turbulent residual layer and a nocturnal stable boundary layer. The mixed layer can be divided into a cloud layer and a subcloud layer (Stull, 1988).

The **surface layer** (SL) characterizes the bottom of the PBL. It is determined by a decreasing moisture with height and a strong wind shear where plumes and dust devils can develop.

In the **mixed layer** (ML) the turbulence is caused by convection (convective mixed layer). This intense vertical mixing implicates that conserved variables like potential temperature and humidity are nearly constant with height. The mixed layer growth is influenced by solar heating of the ground during cloud-free days. A turbulent ML begins to grow in depth about half an hour after sunrise and reaches its maximum depth in the late afternoon. Furthermore, if there are clouds in the ML, it can be distinguished between cloud layer and subcloud layer.

The **residual layer** (RL) is the resulting layer when turbulent air decays in the formerly well-mixed layer and thermals ceases in the absence of cold air advection half an hour before sunset. Passive tracers like aerosols which were dispersed into the daytime mixed layer remain in the RL during night.

The **stable boundary layer** (SBL) forms at night (nocturnal boundary layer, NBL). In urban areas, the ML can continue through the night because of the heat capacity of buildings and streets. The PBL gets stratified whenever the surface is cooler than the ambient air. The greatest static stability can be found near the ground and decreases smoothly towards a neutral height (temperature inversion or nocturnal inversion).

The **entrainment zone** (EZ) can be quite thick (average of round 40 % of the depth of ML). This region is at the top of the ML where there is an entrainment of air downward and an upward transport of air from the ML into the free atmosphere.

4.1.2 Determination of the PBL height with lidar

The lidar permits the detection of the PBL height with a vertical resolution of a few meters and a temporal resolution in the range of seconds to minutes. The observation is possible over longer periods. The determination of the PBL follows the gradient method (e.g., Baars et al. (2008)). This method assumes that the PBL contains much more aerosol than the free troposphere so that a strong decrease of the backscatter signal is observed at the PBL height. In this method, the first derivative of the corrected lidar signal is used. So the minimum gradient indicates the height of the PBL.

Moreover, Groß et al. (2011a) found that there is a sharp decrease of relative humidity and change of extensive and intensive optical properties in their respective vertical profiles at the PBL top.

4.2 Typical weather conditions at Israel

The aerosol transport to Israel is governed by seasonal variations caused by characteristic weather conditions. Dayan et al. (2007) quantify the seasonal distribution of dust observations and accumulated dust based on observations in Beer Sheba in the South of Israel between 1967 and 2003. In Fig. 4.2a is shown that dust events occur rarely in summer (June to September). Most dust events occur from December to May, which is defined as the dust season by the authors. This is caused by synoptic systems in the Mediterranean region. Dayan et al. (2007) correlate the dust events with synoptic systems which dominate at the time of observation (Fig. 4.2b). The Cyprus Low causes four times more dust events and four times more accumulated dust than the second most common system, the Sharav cyclone. These two frequent pressure systems appear in winter up to spring and characterize the dust season. The Red-Sea trough influences the dust in a similar strong way as the Sharav cyclone. On the other hand, an high pressure system over Israel and an high east of Israel and the Persian trough influence the dust concentration in Israel less.

The following explanation of the three important synoptic systems is based on the publi-

cation by Dayan et al. (2007).

During the Cyprus low, there is a low pressure system over Turkey or over Cyprus. Due to the cyclonic flow, moist air masses which cause numerous precipitation are transported eastward over the Mediterranean Sea to Israel.

The name of the Sharav cyclone is based on the desert wind Sharav which influences the eastern Mediterranean area. In general, one low pressure system is located over northern Egypt and a second one over southern Turkey. The southerly cyclonic flow leads to dry air masses which were transported from the Saharan Desert and to little precipitation in Israel. Sharav cyclones occur during spring and summer time. Furthermore, the highest temperatures of the whole year can be achieved in the eastern Mediterranean area during this weather condition.

The Red-Sea trough, as the westward expansion of the Asian summer monsoon causes floods in the south-eastern Mediterranean area (Osetinsky, 2006). It is a low pressure system or a trough over the Red Sea and the air flow comes from the east (Middle East).

Additionally, the weather situation is often influenced by a subtropical high in Israel during summer (Dayan and Rodnizki, 1999).

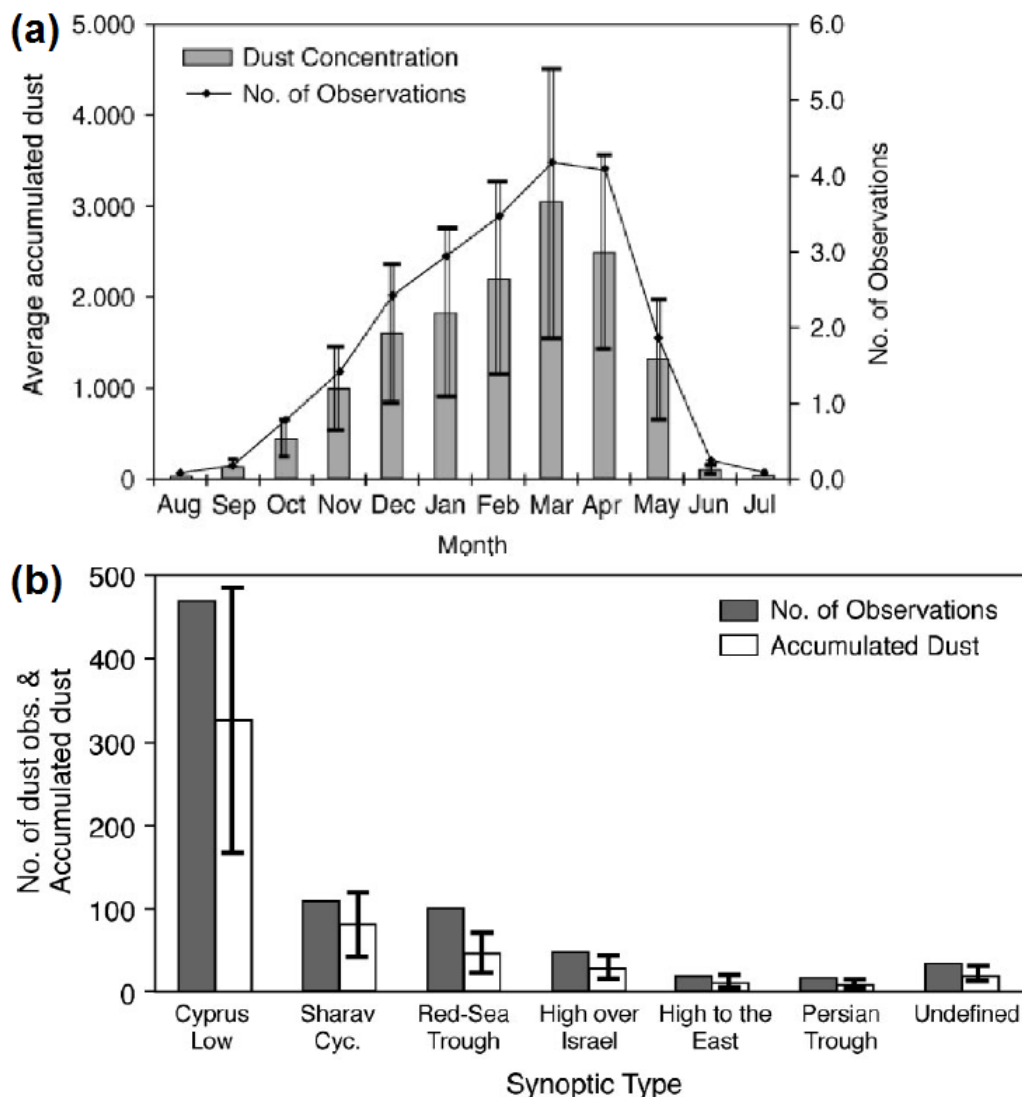


Figure 4.2: Monthly distribution of the average accumulated dust (columns) and number of observations (line) at the site Beer Sheba (a). The dust distribution among the synoptic systems is demonstrated by the number of dust observations and the accumulated dust (b). The measurements were taken from 1967 to 2003 (Dayan et al., 2007).

4.3 Land and sea breeze

Haifa is located at the coast of the Mediterranean Sea. So the land sea breeze influences the evolution of the planetary boundary layer and the distribution of aerosols. Ganor et al. (1998) investigated individual aerosol particles which had been collected on board a ship in the Haifa Bay during August in the years 1987 and 1995. They analyzed the

constituents of particles occur due to sea or land breeze and determined their chemical components by electron microscopy. During land breeze, more particles were detected than during sea breeze. The particles which were identified as local aerosol during land breeze are characterized by phosphate, fly ash and soil particles.

The idealized land sea breeze circulation is shown in detail in Fig. 4.3.

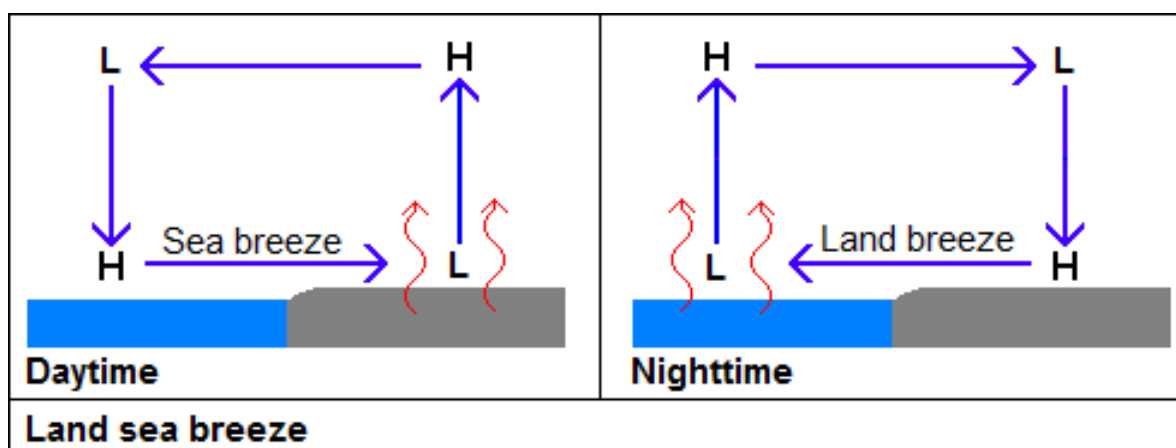


Figure 4.3: Illustration showing the land sea breeze during day and night (Forkel, 2015).

During the day, the land's surface heats up more than the sea by solar radiation due to the different heat capacity of the ground and sea. That's why the air over land rises and develops lower air pressure in relation to the air over the sea. A so called sea breeze, which cools the coast, balances out these pressure differences during daytime. During night, the air flow is in the opposite direction (land breeze). The land mass cools faster than the sea due to different heat capacity of land and water. The air rises over the sea and consequently low air pressure occurs there. So a balancing current blows towards the sea, originating from land (higher air pressure) (Forkel, 2015).

Applied for Haifa, a sea breeze would flow from north west during daytime and a land breeze from south east in the night. But the coast and the orography of Haifa is complex because of various hills and a non-straight coastline. Therefore, the land and sea breeze is not well established in Haifa.

5 Measurement examples

The measurements with Polly^{XT} are taking place at Technion in Haifa (32.776 N, 35.025 E) since March 2017. The measuring period relevant for this study is from March 2017 to September 2017. The measurement location is near a hill and has an elevation of 230 m above sea level.

This chapter describes three case studies. Firstly, the development of the planetary boundary layer is compared with the theoretical basics of Stull (1988). Secondly, a record of land sea breeze is shown. The third case study of a typical aerosol measurement presents a particular dust case.

5.1 Development of the PBL on 4 April 2017

The temporal development of the uncalibrated attenuated backscatter coefficient shows that some structures of the PBL are developed before sunrise (Fig. 5.1) and lowered until sunrise down to 1000 m. Furthermore, a thin aerosol layer is detected between 3000 and 4000 m, but this will not be taken into account in this consideration. At sunrise, the PBL height is close to the surface layer and no gradient is identifiable between 300 and 1500 m in the particle backscatter profile. The air temperature range was between 12 °C and 23 °C on that day (WeatherUnderground-April, 2018). Around 7 UTC (10 LT) convection starts and the development of the mixed layer (ML) was undisturbed by clouds. Shortly before sunset, the ML reaches its maximum height of 2000 m.

Furthermore, the entrainment zone has not developed during the measuring period. The surface layer height which is lower than 200 m cannot be seen in the lidar measurements because this height is below the overlap of the near-range channels.

Most of the ML decreases after sunset. It is found that the residual layer (RL) has developed and reaches its maximum height of nearly 2500 m at 18 UTC. The RL remains until 0 UTC (3 LT) and does not vary its maximum height. The stable boundary layer is observed below 1000 m from midnight.

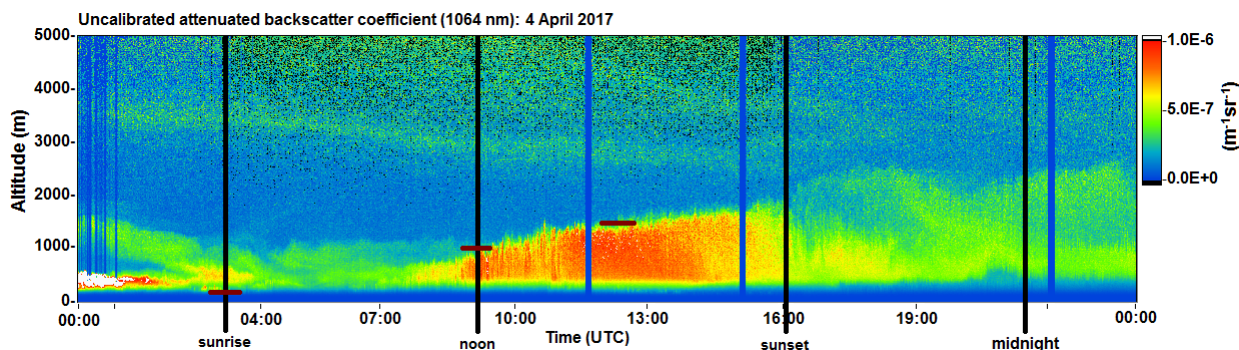


Figure 5.1: Uncalibrated attenuated backscatter coefficient (1064 nm) from 04.04.2017 with marked time of sunrise (06:23 LT, 03:23 UTC), noon (12:42 LT, 09:42 UTC), sunset (19:02 LT, 16:02 UTC) and midnight as well as determined heights of PBL (brown lines).

5.2 Record of land sea breeze

Ganor et al. (1998) have examined individual atmospheric particles at the Israeli coast and which atmospheric particles occurred during land or sea breeze measuring on board a ship. They found out that more particles were detected during land breeze than during sea breeze.

Now the land sea breeze is investigated with lidar. An important factor for detection this circulation is the wind leap. Hence, records of Haifa University (<https://ims.data.gov.il/>) about the wind direction and wind speed are used to identify land sea breeze events. Only wind leaps of more than 90 degrees were considered and the lidar measuring periods were chosen shortly before and after those wind leaps. Figure 5.2 shows the case of 27 May 2017. Before the wind leap (07:23-08:21 UTC), the wind direction was around 50° (north-east) and 225° (south-west) in the late afternoon and stayed nearly constant till the end of day. The wind velocity was between 0 and 5.8 ms^{-1} during the day and between 3 and 4 ms^{-1} during each lidar measuring period.

Figure 5.3 shows a temporal development of the uncalibrated attenuated backscatter coefficient for the whole day. First, the intensive properties of aerosol particles are checked to examine, whether the particle composition has changed. Calculations of the backscatter coefficient, Ångström exponent (355/532 nm) and the depolarization ratio at 532 nm for both time periods are shown in Fig. 5.4. The particle backscatter coefficient is larger between 1.6 and 2.6 km before the wind leap. So less particles stayed in these heights

after the wind leap. Below 1.5 km, more particles are detected after the wind leap. The vertical profile of the particle depolarization ratio (green line) shows a vertical mixed atmosphere between 1 and 3 km because values of the particle depolarization ratio are equal within these heights. Before the wind leap, the values of the Ångström exponent are larger. That's why the atmosphere was perhaps influenced by smaller particles before the wind leap.

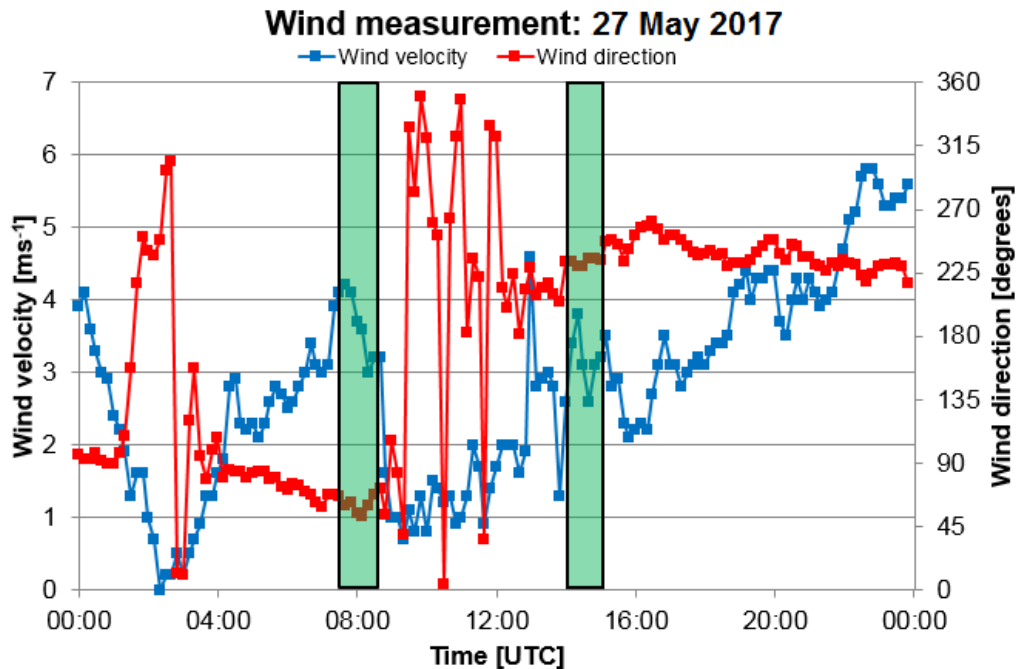


Figure 5.2: Measurement of wind velocity (blue line) and wind direction (red line) at Haifa University (<https://ims.data.gov.il/>) on 27 May 2017. The two green boxes mark the lidar measurement before (07:23-08:21 UTC, 10:23-11:21 LT) and after (14:00-15:00 UTC, 17:00-18:00 LT) the wind leap.

The land sea breeze is difficult to detect with lidar because the lidar data have an incomplete overlap below 600 m when evaluated by the Klett method during daytime. Therefore, it is difficult to examine this circulation which takes place in a height range of 1500-3000 ft (457-914 m) above sea level (Pfeffer, 2017). The lidar has an elevation of 230 m and so the circulation is nearly complete in the height range of the overlap. Also the coast line is very inhomogeneous because of many different orographic factors and hence there is no direct theoretical description of the land sea breeze feature available. In contrast to the measurements of Ganor et al. (1998), the lidar measurements, described in this study, took place on a hill instead on board a ship. As a consequence, important information at the lowest heights cannot be obtained for this small scale circulation.

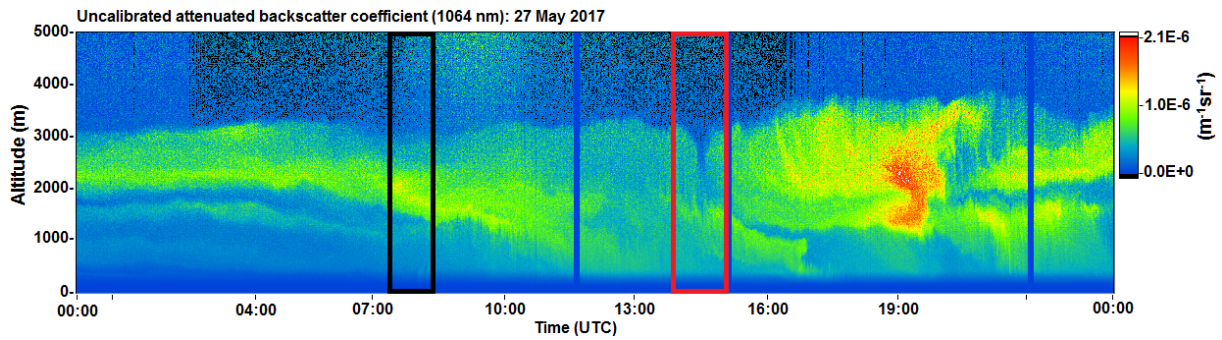


Figure 5.3: Uncalibrated attenuated backscatter coefficient (1064 nm) on 27 May 2017 with investigation period from 07:23-08:21 UTC (before the wind leap, black box) and from 14:00-15:00 UTC (after the wind leap, red box).

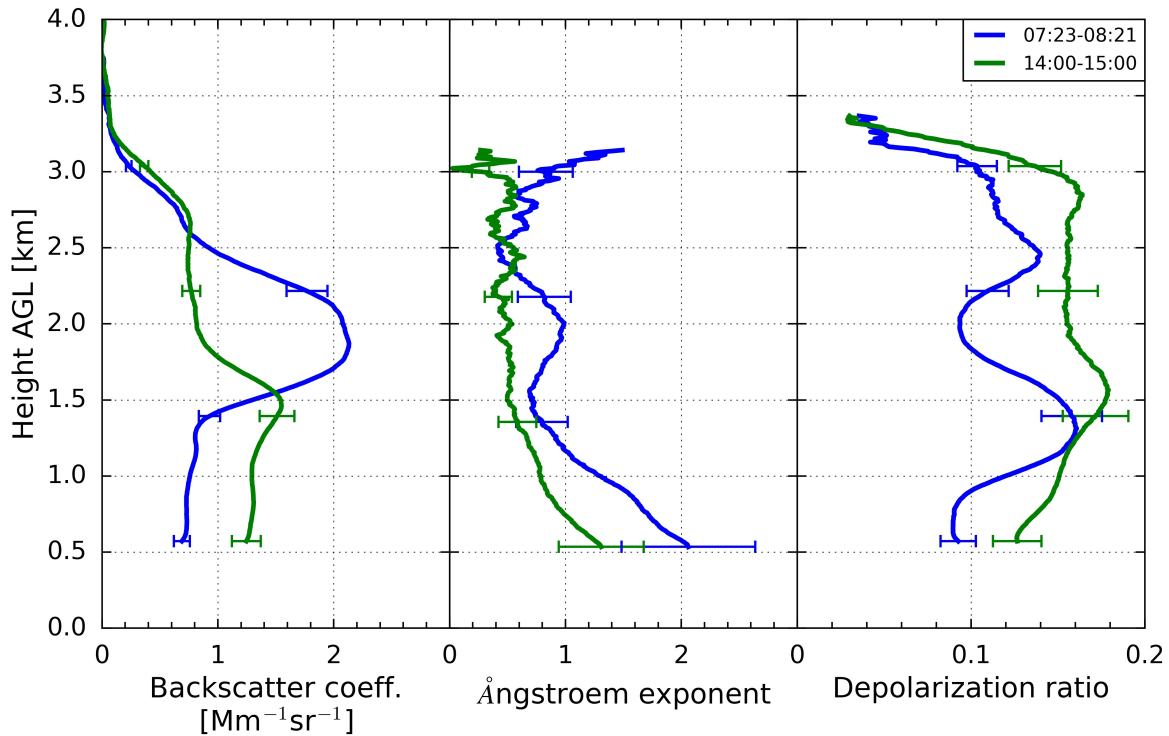


Figure 5.4: Vertical profiles of particle backscatter coefficient (532 nm), Ångström exponent (355/532 nm) and particle depolarization ratio (532 nm) for 27 May 2017 07:23-08:21 UTC (before the wind leap, blue line) and 14:00-15:00 UTC (after the wind leap, green line). The error bar calculation is based on Hofer et al. (2017).

5.3 Aerosol layer on 9 June 2017

This case study describes a dust event on 9 June 2017. Figure 5.5 shows an aerosol layer that reaches up to 4000 m. In the beginning of the day, the layer is less homogeneous than during the chosen measuring period (red box in Fig. 5.5), where the aerosol layer ranges from 1000 to 3000 m and is sharply separated from the above and below height levels.

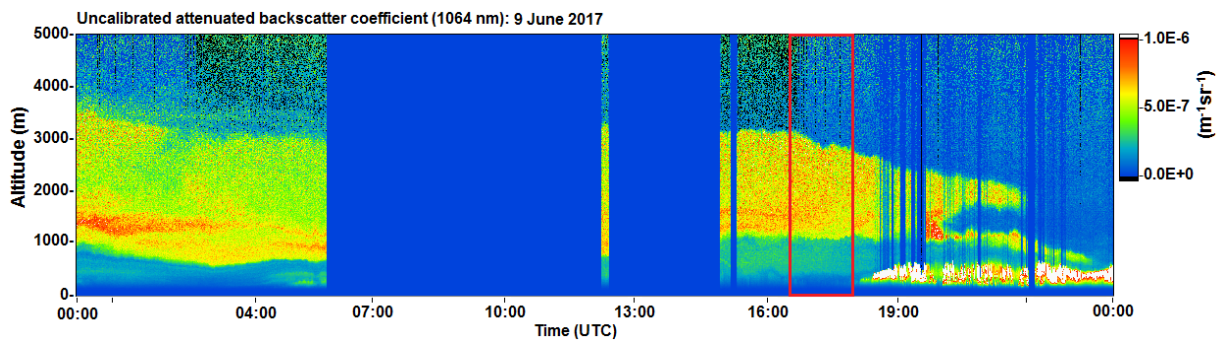


Figure 5.5: Uncalibrated attenuated backscatter coefficient (1064 nm) on 9 June 2017 with red box from 16:45-17:58 UTC indicating the averaging time of the profiles in Fig. 5.6.

The derived profiles of intensive and extensive quantities which were evaluated with the Raman method display a decrease in the vertical profile of the particle backscatter coefficient and depolarization ratio (Fig. 5.6). The depolarization ratio is larger than 0.2, so this aerosol has a large size and a non-spherical shape according to the introduced aerosol type identification. Following Tesche et al. (2009), the determined lidar ratio of 55 sr (532 nm), averaged between 1500 and 2500 m, indicates mineral dust from the Saharan desert in the aerosol layer around 2000 m. The extinction related Ångström exponent is close to zero in the considered height range which suggests Saharan dust as well (Baars et al., 2016). Also the Poliphon calculation shows a maximum mass concentration for dust of $75 \mu\text{g m}^{-3}$ between 1500 and 2500 m (yellow line).

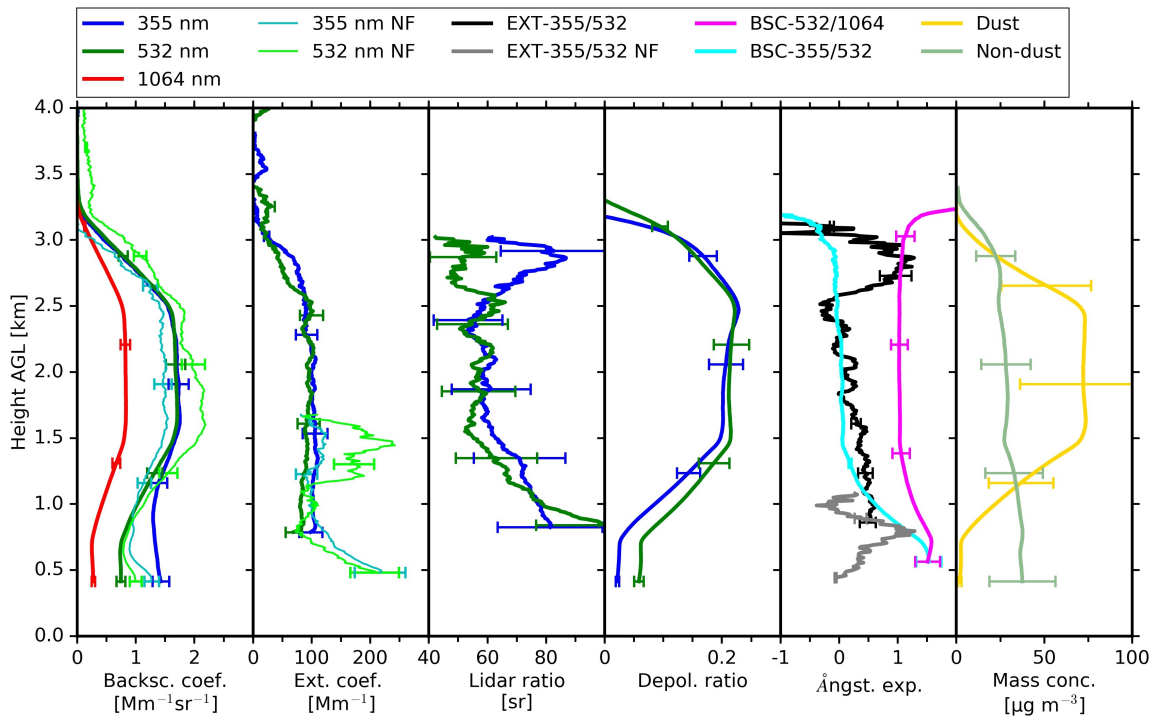


Figure 5.6: Vertical profiles of the particle backscatter coefficient, particle extinction coefficient, lidar ratio, linear depolarization ratio, Ångström exponent and mass concentration for the respective wavelengths on 9 June 2017 16:45-17:58 UTC. The error bar calculations are based on Hofer et al. (2017).

HYSPLIT was used to assess the origin of the aerosol calculating backward trajectories for three levels (1300, 2000 and 2800 m AGL). These heights are roughly the center, the upper and lower boundary of the layer. The calculation has a duration of 114 hours (Fig. 5.7) because the three trajectories end below 1000 m which could be within a possible PBL height in this region. All three trajectories indicate that the air masses were coming from the desert areas in the south of Libya and Egypt and it is likely that they contain Saharan dust.

The second calculation using FLEXPART investigates which areas did act as source regions of the observed aerosol between 1300 and 2700 m height. The result (Fig. 5.8) shows that those air parcels had their residence time below 3 km mostly in the whole north-east region of Africa (Egypt, Algeria) and at the south-west coast of Turkey.

The meteorological condition is shown using GFS (Global Forecast System) model output at the 700 hPa geopotential height. A low air pressure system in 700 hPa is observed that is located over the Mediterranean Sea north of Libya and south of Greece on 7 June 2017 (Fig. 5.9a). The low pressure system came from west and moved north-eastward to

Turkey until 9 June 2017. The highest wind speed from a westerly direction is generated at the south and south-east side of the pressure system. The wind speed is over 6 ms^{-1} in this area, so uplifting of mineral dust particles is possible. That's why the Saharan dust was transported in a low pressure system from North Africa north-eastward towards Haifa.

This event shows a pronounced dust layer. The profiles of the intensive and extensive quantities are constant with height within this layer. Moreover, the measured values of the lidar ratio, particle depolarization ratio and Ångström exponent correspond to the measured values for Saharan dust during different campaigns (Tesche et al., 2009; Baars et al., 2016).

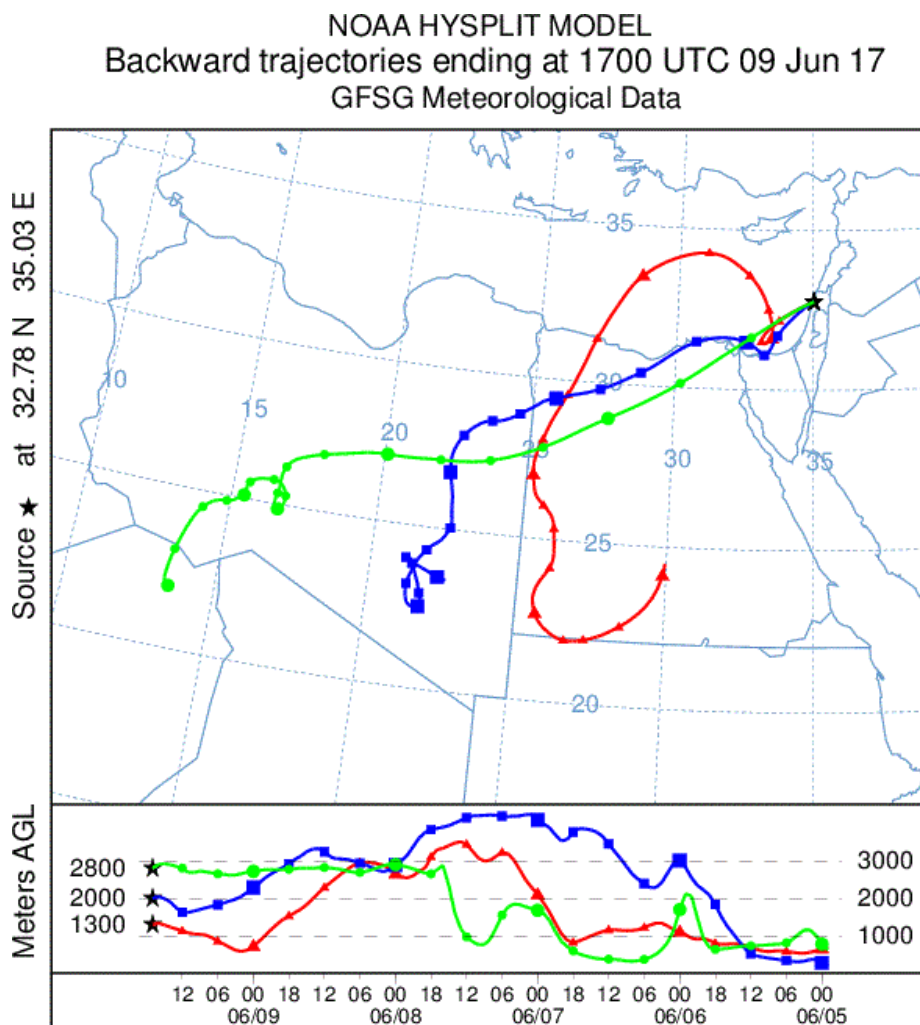


Figure 5.7: NOAA HYSPLIT model backward trajectories for Haifa (32.78 N, 35.03 E) at 9 June 2017 17 UTC. Three heights have been calculated (1300, 2000, 2800 m AGL) for a duration of 114 hours.

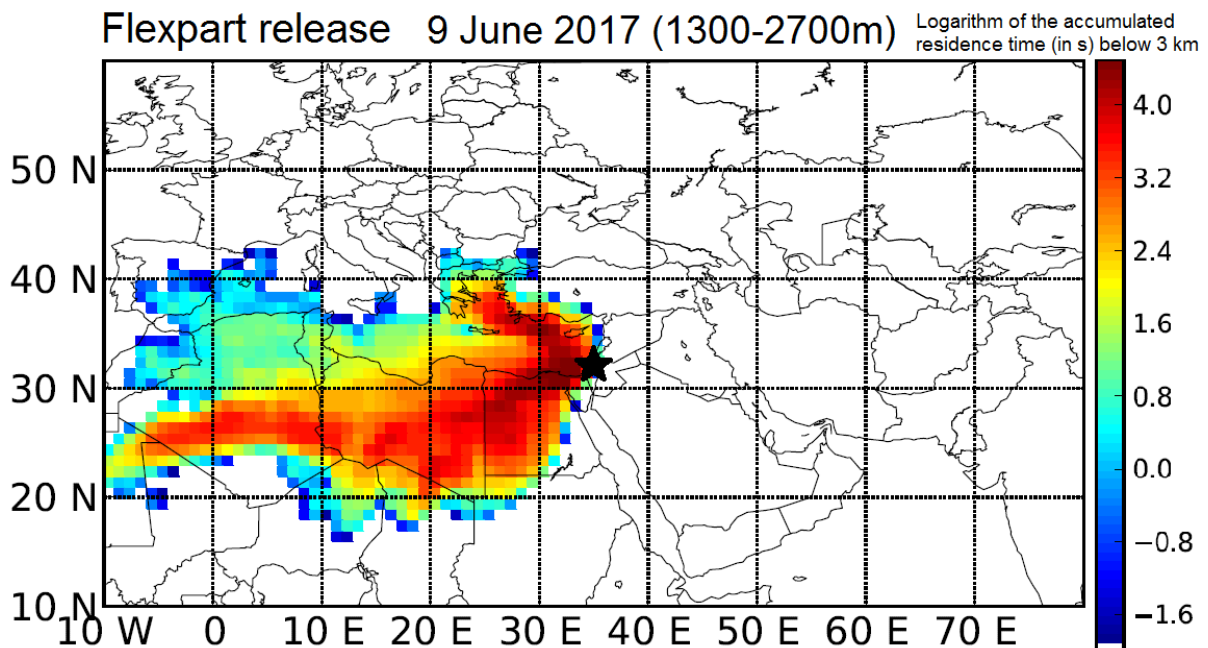
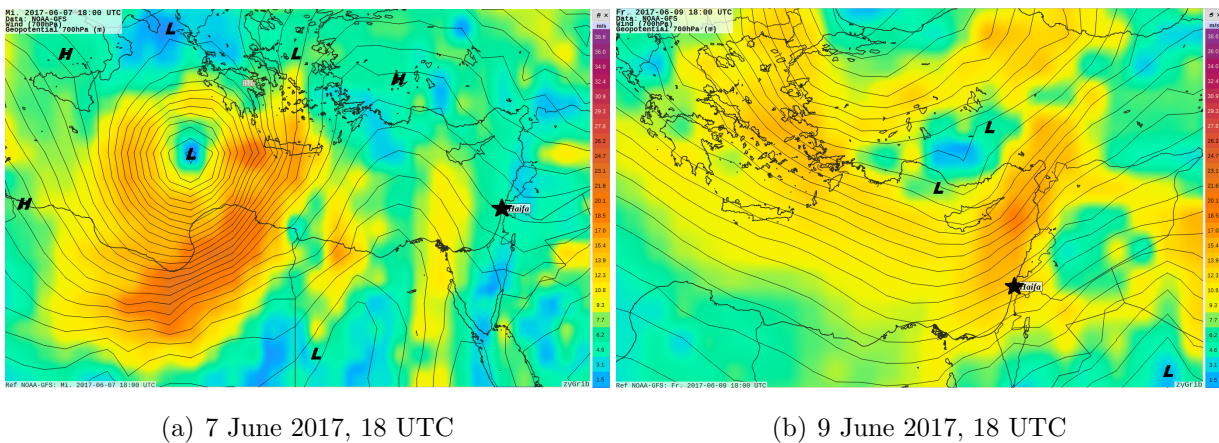


Figure 5.8: Model calculation FLEXPART for 9 June 2017 for the height range from 1300 to 2700 m. The computation was done for 4 days backwards. The color bar scale is the logarithm of the accumulated residence time below 3 km of trajectories ending in Haifa.



(a) 7 June 2017, 18 UTC

(b) 9 June 2017, 18 UTC

Figure 5.9: Isohyps 700 hPa geopotential (≈ 3000 m) with spacing of 5 hPa. Colors represent the wind speed at 700 hPa (blue ≈ 2 ms^{-1} , green ≈ 7 ms^{-1} , yellow ≈ 10 ms^{-1} , orange ≈ 16 ms^{-1} , red ≈ 22 ms^{-1}). This GFS model output from NOAA (National Oceanic and Atmospheric Administration) is visualized with the program "zyGrib" (www.zygrib.org).

6 Classification of aerosol layers

This study of the vertical aerosol distributions is based on 107 manually analyzed lidar profiles. They were calculated with the Raman method because the uncertainties of the overlap effect are smaller. The measuring periods of the respective data were often in the evening, shortly after sunset within cloud-free conditions or sometimes shortly before sunrise, when clouds had disappeared. Usually, the profiles were evaluated for periods between one and two hours and during homogeneous conditions. For June to September, one measuring period per day was evaluated in case of a cloud-free evening or night. There is more than one Raman evaluation available per day for April and May because the profiles were already analyzed for another project.

The resulting aerosol layers are defined by visual inspection of the range-corrected signals and the vertical profiles of the particle backscatter coefficient using the gradient method (Sect. 4.1.2). The aerosol layers which are counted from the ground to the uppermost height, starting with the PBL, are the basis for part (a) of the following plots. At maximum, three aerosol layers are detected above the PBL. This results in the subdivision of the planetary boundary layer, a first layer, a second layer and a third layer. In the following, these layer classes are named as PBL, Layer 1, Layer 2 and Layer 3. Each of these layers represents a height range and a layer thickness.

These layers are allocated in intervals from below 500 m up to 9000 m with widths of 500 m. It happened that the PBL is found to be below 250 m height and the lower boundary of Layer 1 is also in the interval below 500 m. Consequently, there might be more detected aerosol types (variable m) in the lowest 500 m interval than the number of evaluations n . To compare the entire height interval in the plots, the number of each height interval is normalized by the number m of the aerosol types in the lowest layer to get 100%. If the same aerosol type occurs in two layers and in the same height interval in one evaluation, the differentiation of aerosol types will not be made. In part (b) of the following plots, this fact is illustrated in the layer height ranges.

The red boxes define the second and third quartile of the data (25 to 75% of all data). The lower line defines the first quartile with 0 to 25% of the data in smaller heights and the upper line characterizes the fourth quartile with 75 to 100% of the data in larger

heights. It can be seen on the basis of the red boxes in which height ranges most of the counted layers are located for each month and how the different layers overlay each other. On this basis, the intensive and extensive quantities (Table 6.1) are determined for all layers. These quantities have already been discussed for the aerosol layer on 9 June 2017 in Sect. 5.3.

Table 6.1: Manually recorded quantities for each aerosol layer.

Wavelength [nm]	Available values for the counted layers (PBL, Layer 1, Layer 2, Layer 3)
355, 532	height range, geometric height, height of maximum scattering; β (maximum), α (maximum), δ_{par} (maximum), δ_{par} (mean), LR (mean)
1064	height range, geometric height, height of maximum scattering; β (maximum)
	extinction-related Ångström exponent, backscatter-related Ångström exponent: $\mathring{A}_{355-1064}$, $\mathring{A}_{532-1064}$, $\mathring{A}_{355-532}$

The respective layer heights are determined with the particle backscatter coefficient β at 532 nm wavelength (c.f., Sect. 4.1.2). The maximum value of the linear particle depolarization ratio δ_{par}^{532} and the Ångström exponent $\mathring{A}_{532-1064}$ of the respective layers are used for the aerosol type characterization (Baars et al. (2017), Sect. 3.2). The monthly overviews show all aerosol types which were detected in the respective heights (part (a) of the following figures). The data are available on request from `dietrich@tropos.de`.

March 2017

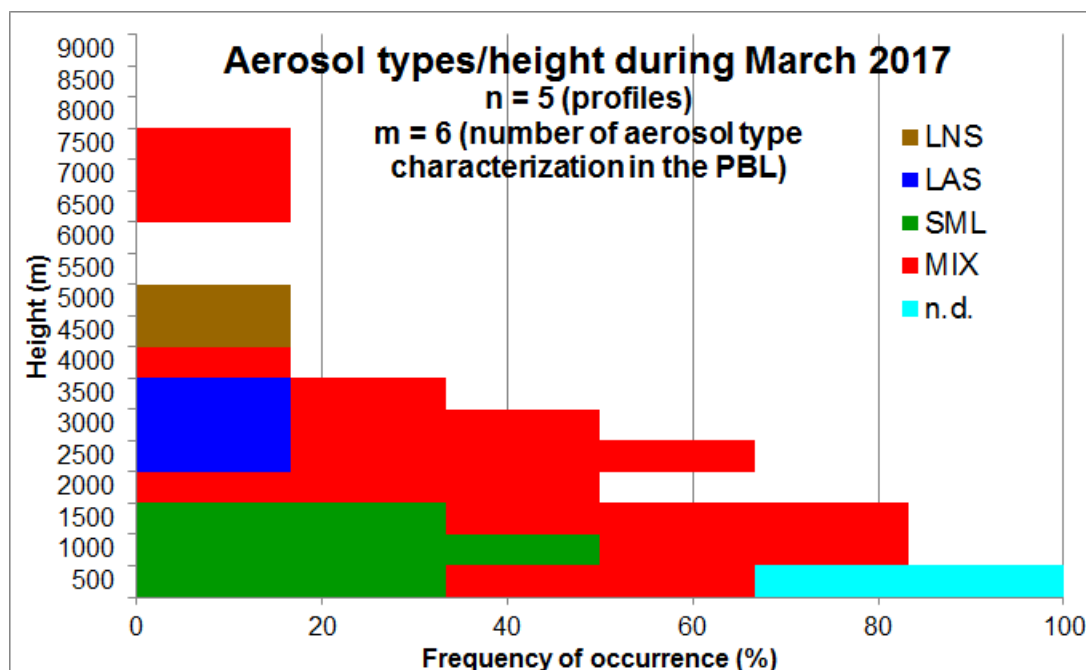
The statistic of this month is based on only 5 profiles. For March, the aerosol types "small" (SML) and "aerosol mix" (MIX), besides "not definable" are equally distributed in the lowest height (Fig. 6.1a). MIX occurs most frequently up to a height of 4000 m. Furthermore, MIX is also found between 6500 and 7500 m. An aerosol layer was detected between 4500 and 5000 m which is characterized as large non-spherical (LNS). One dust layer occurred above Haifa during March 2017, too. One layer of large spherical aerosol (LAS) was also observed between 2500 and 3000 m.

Individual PBL heights reach up to heights of 1600 m, but 75% of all PBL heights are below or equal to 500 m (Fig. 6.1b). In addition, the outermost quartiles of Layer 1 and 2 overlap each other and a third layer was counted once for this month.

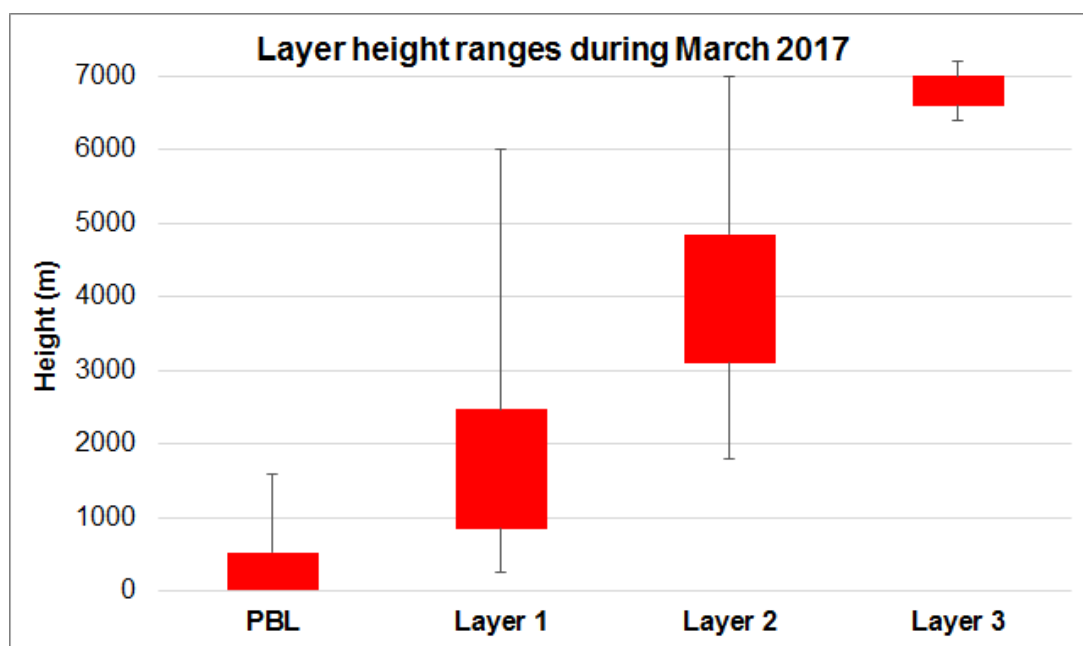
April 2017

The analyses for April are based on 9 profiles. The aerosol distribution is mainly characterized by MIX and LNS (Fig. 6.2a). LNS reaches up to 5500 m and has a maximum occurrence of around 27%. In contrast to this, MIX rises to 7000 m, the distribution thins out to upper heights and is largest below 2000 m (45% occurrence). A possible reason might be the weather conditions. High and low pressure systems are found in the pressure level of 500 hPa (\approx 5500 m) in the dates with air flows from the south-west and south-east. LNS and other atmospheric particles are transported LNS to Haifa, got mixed, and were detected as MIX by the lidar. Also SML occurs up to 1000 m which might be caused by the local urban area and industries in the surrounds of Haifa.

No third layer is counted for April (Fig. 6.2b). Layer 1 extends between 250 and 6000 m, but this large range of Layer 1 has been detected in one profile. This aerosol layer on 12 April 2017 0:25-2:00 UTC extended between 1100 and 6000 m. Layer 2 is between 5000 and 7000 m and contains of one case.

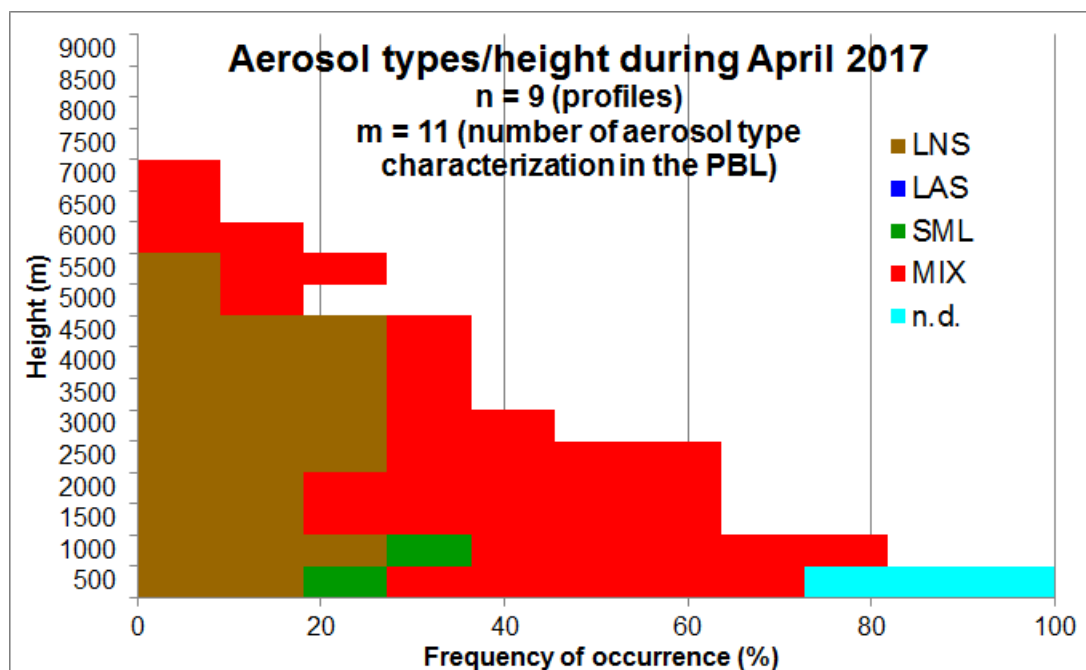


(a) Frequency of occurrence per interval of the aerosol types in March 2017. The height intervals are divided into 500 m bins. For example 500 m means every height between 1 and 500 m and 1000 m is 501 to 1000 m and so on.

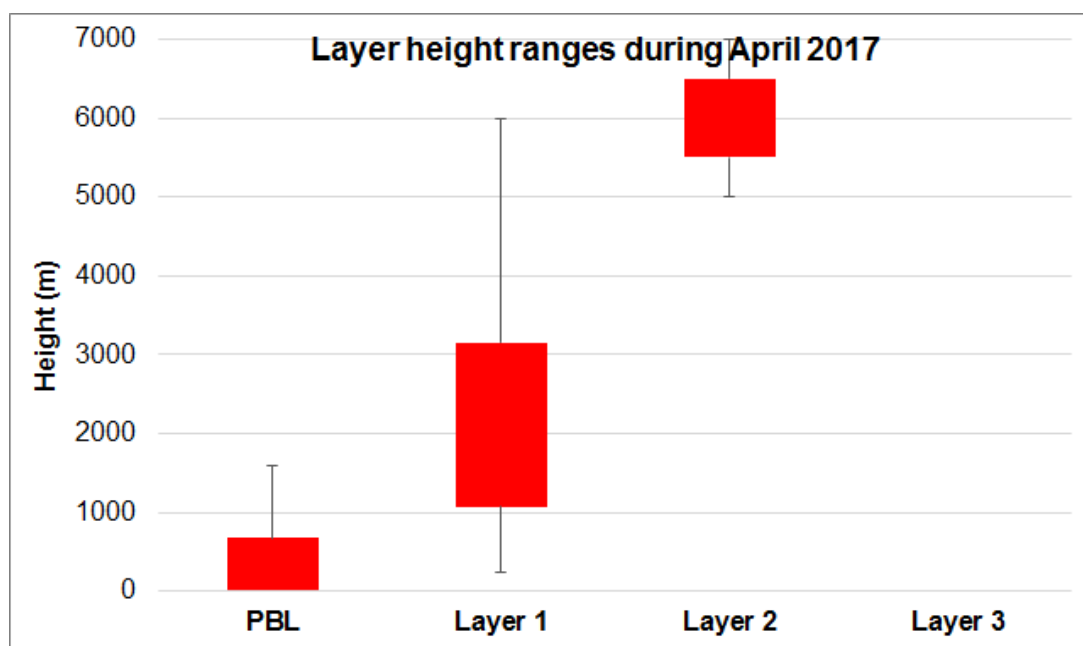


(b) Height ranges which are covered by the layers in March 2017 (PBL, Layer 1, Layer 2, Layer 3). The upper boundary of the red box marks 75% of the data and the lower boundary shows 25% of the data.

Figure 6.1: Aerosol types per interval and layer height ranges for March 2017.



(a) Frequency of occurrence per interval of the aerosol types in April 2017. The height intervals are divided into 500 m bins. For example 500 m means every height between 1 and 500 m and 1000 m is 501 to 1000 m and so on.



(b) Height ranges which are covered by the layers in April 2017 (PBL, Layer 1, Layer 2, Layer 3). The upper boundary of the red box marks 75% of the data and the lower boundary shows 25% of the data.

Figure 6.2: Aerosol types per interval and layer height ranges for April 2017.

May 2017

The statistics for May is compiled from 16 profiles of 11 different days. In 38% of all cases below 500 m, the aerosol type could not be matched to LNS, LAS, SML and MIX (Fig. 6.3a). This is caused by a PBL height below 250 m. Therefore, reliable values of the intensive and extensive, optical quantities could not be determined. This goes hand in hand with the fact that 75% of all data is below a height of 262 m and only some isolated cases (fourth quartile) lead to larger heights (Fig. 6.3b).

May is the only month where aerosol types occurred up to 9000 m. MIX is detected in all height levels and thins out in upper heights. It occurs in about $\frac{1}{3}$ of all profiles at heights below 2000 m and in 4 to 17% of all profiles at heights above 2500 m. Furthermore, SML was only measured up to a height of 2000 m in May. Additionally, LNS is observed at all height levels below 7500 m with a maximum occurrence of 17% between 2500 and 4000 m. There were no characteristic ground pressure conditions observed for May 2017. But a westerly and south-westerly flow in the 500 hPa level may have transported dust and aerosol mix towards Haifa.

Layer 1 has many outliers upwards above the height of 1700 m, the upper 25% of the data (fourth quartile) (Fig. 6.3b). Layer 3 has also many outliers, but downwards where the first quartile (lower 25% of the data) is between 2000 and 5000 m. Layer 2 was counted in the height ranges between 1000 and 6000 m and all cases have nearly the same vertical extensions.

June 2017

On the basis of 23 profiles (Fig. 6.4a), it is shown that the aerosol distribution reaches only up to 5000 m except for one case. LNS is rarely observed in June and LAS occurs in 6% of the profiles below 500 m. MIX reaches 29% between 2000 and 2500 m, and 3% and 16% in the lower and upper heights. SML and its distribution is significant for June. This type reaches its maximum of 58% in the height ranges below 1000 m and extends up to 4000 m. There were only weak high pressure systems observed during June 2017 that have affected the weather in Haifa during in this month. Therefore, the influence of the metropolitan region of Haifa is dominant. Hence, on the one hand, small aerosol particles emitted by factories are found and on the other hand, LNS has been mixed with these particles causing the detected MIX aerosol.

Figure 6.4 (b) shows that the fourth quartile of Layer 1 and the first quartile of Layer 2 overlap each other. Some of the cases in Layer 1 have a large vertical extension. In

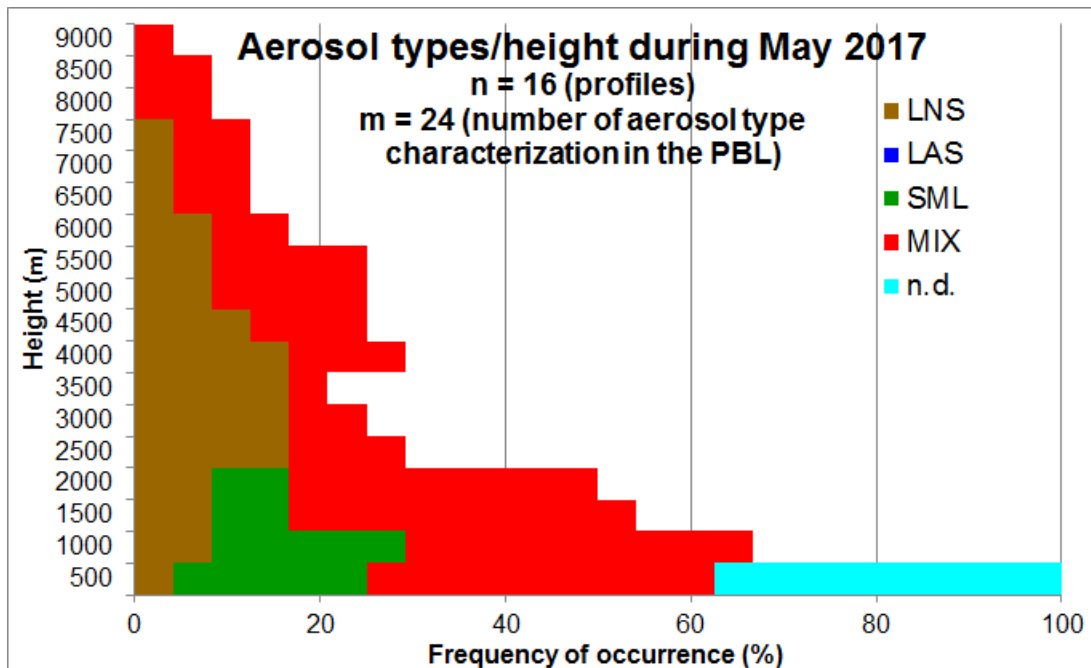
contrast to this, there are thin, first counted layers followed by Layer 2. Layer 3 has a very small range from 3100 to 4100 m. If a Layer 3 is counted, the underlying layers have a small vertical extension.

July 2017

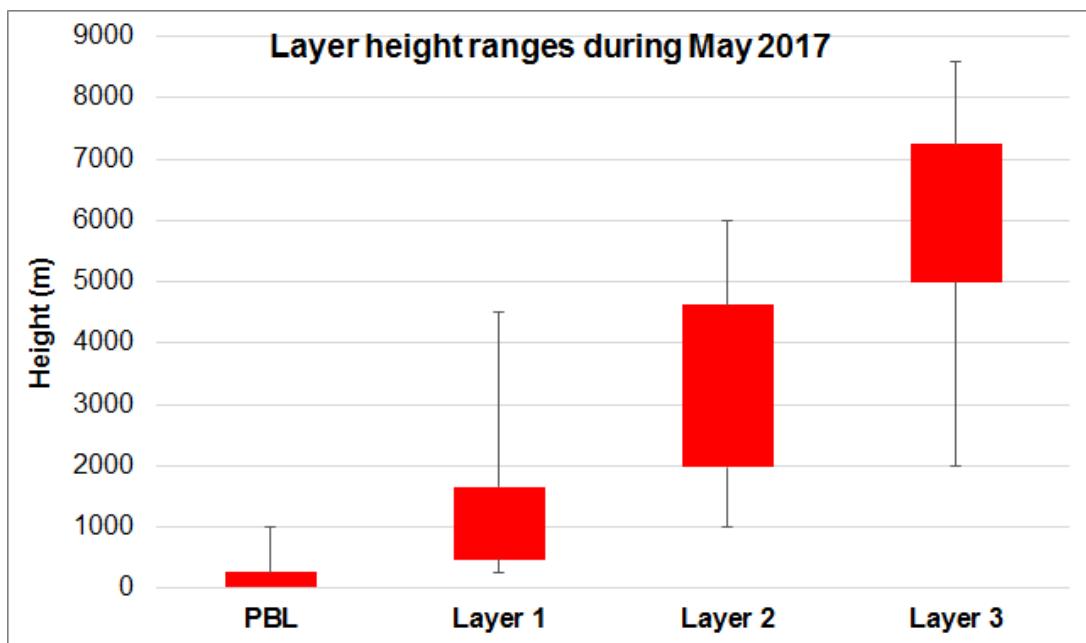
A strong influence of MIX is visible for July, which is based on 24 profiles (Fig. 6.5a). This aerosol type is evident in more than 50% of all cases up to a height of 4000 m and has a maximum occurrence of 82% in the height ranges below 1000 m. Moreover, MIX is detected up to 7000 m. LNS is determined between 1500 and 6000 m and its maximum occurrence is smaller than 11%. SML is identified below 1000 m and has a significantly higher occurrence than MIX (55% for SML and 16% for MIX).

Because of the subtropical high, the eastern Mediterranean area was influenced by stable weather conditions. Therefore, only aerosol from the surrounding area has been observed. So it is possible that SML and LNS have been mixed.

It is obvious that no Layer 3 was established in July (Fig. 6.5b). The red boxes of Layer 1 and 2 do not overlap each other, but the fourth quartile of Layer 1 and the first quartile of Layer 2 have overlays because some cases in Layer 1 have a large vertical extension in the overlaying range. During those measurements, no Layer 2 is counted.

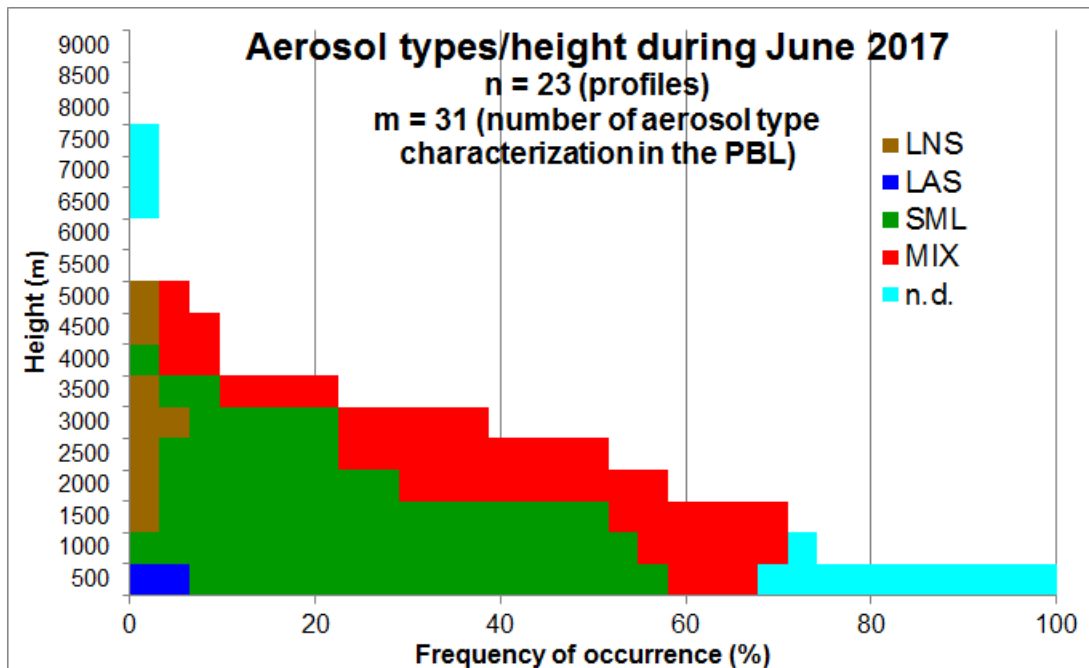


(a) Frequency of occurrence per interval of the aerosol types in May 2017. The height intervals are divided into 500 m bins. For example 500 m means every height between 1 and 500 m and 1000 m is 501 to 1000 m and so on.

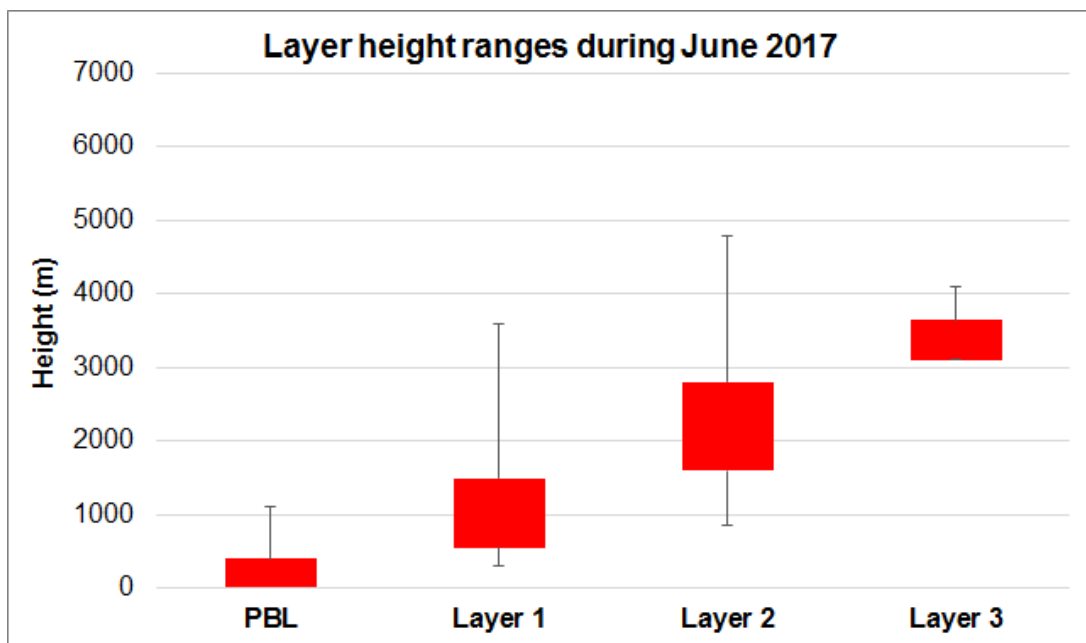


(b) Height ranges which are covered by the layers in May 2017 (PBL, Layer 1, Layer 2, Layer 3). The upper boundary of the red box marks 75% of the data and the lower boundary shows 25% of the data.

Figure 6.3: Aerosol types per interval and layer height ranges for May 2017.

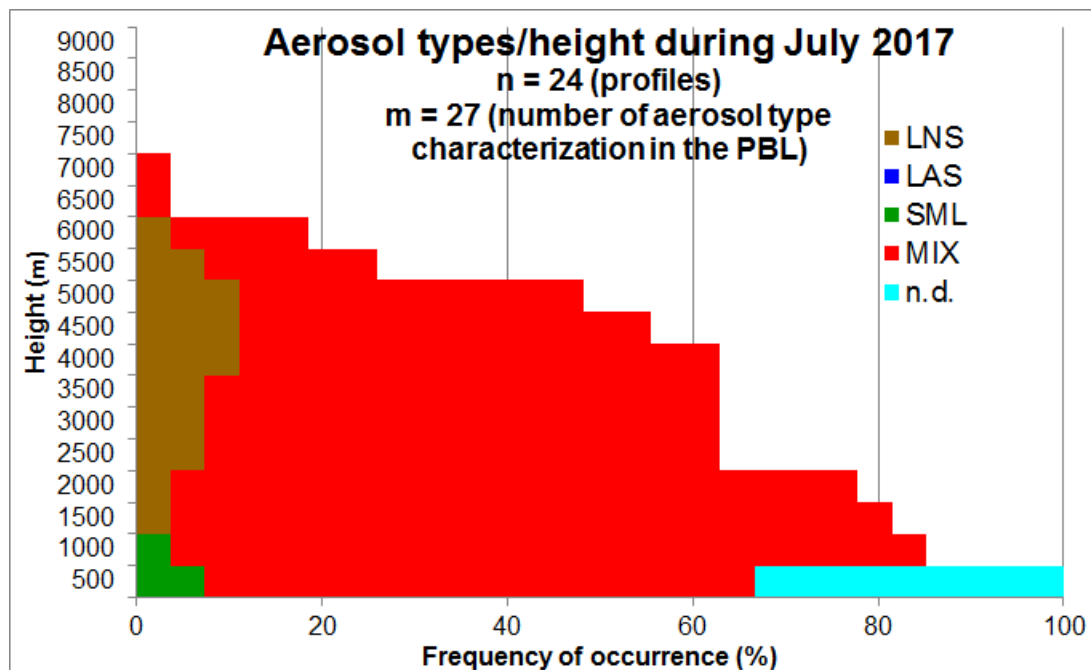


(a) Frequency of occurrence per interval of the aerosol types in June 2017. The height intervals are divided into 500 m bins. For example 500 m means every height between 1 and 500 m and 1000 m is 501 to 1000 m and so on.

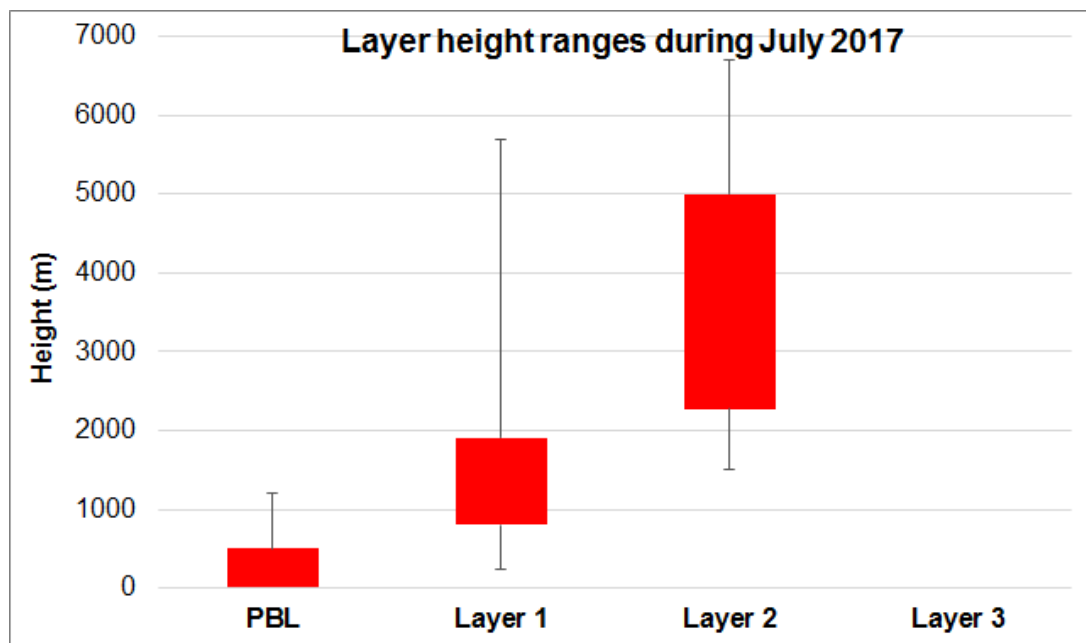


(b) Height ranges which are covered by the layers in June 2017 (PBL, Layer 1, Layer 2, Layer 3). The upper boundary of the red box marks 75% of the data and the lower boundary shows 25% of the data.

Figure 6.4: Aerosol types per interval and layer height ranges for June 2017.



(a) Frequency of occurrence per interval of the aerosol types in July 2017. The height intervals are divided into 500 m bins. For example 500 m means every height between 1 and 500 m and 1000 m is 501 to 1000 m and so on.



(b) Height ranges which are covered by the layers in July 2017 (PBL, Layer 1, Layer 2, Layer 3). The upper boundary of the red box marks 75% of the data and the lower boundary shows 25% of the data.

Figure 6.5: Aerosol types per interval and layer height ranges for July 2017.

August 2017

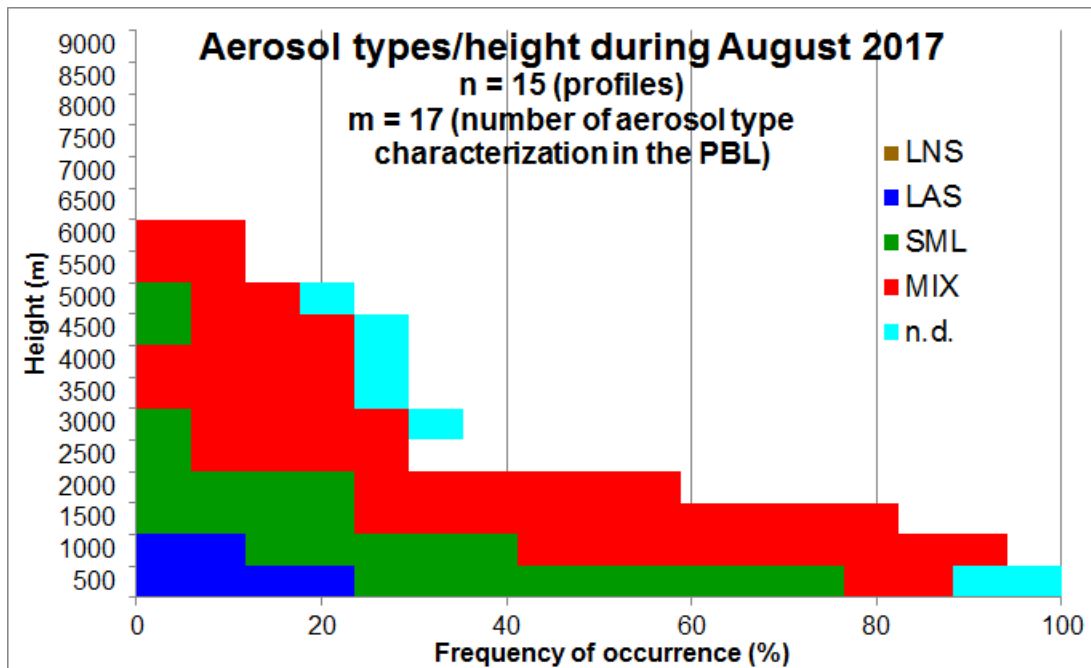
On the basis of 15 profiles, Fig. 6.6 (a) shows that the aerosol layers reach up to 6000 m in August 2017. LAS occurs to heights of 1000 m and it reaches 24% of occurrence below 500 m. The most frequently occurring aerosol types are MIX and SML from the surrounding area. The stability in the weather condition is caused by the subtropical high. SML is detected up to 3000 m and the frequency of occurrence is largest in lower heights (53% below 500 m and 29% below 1000 m). Between 4500 and 5000 m, SML is detected during around 6% of the measurements, as one layer with SML was recorded in one profile. The distribution of MIX ends below 6000 m and a maximum value of 58% is determined in 1500 m height.

The height range from 500 to 5800 m of Layer 2 overlays parts of Layer 1 and the complete Layer 3 (Fig. 6.6b). The underlying layers have a small vertical extension when a Layer 3 was counted in the vertical profiles. The large vertical extension of Layer 2 leads also to a small vertical height range of PBL and Layer 1.

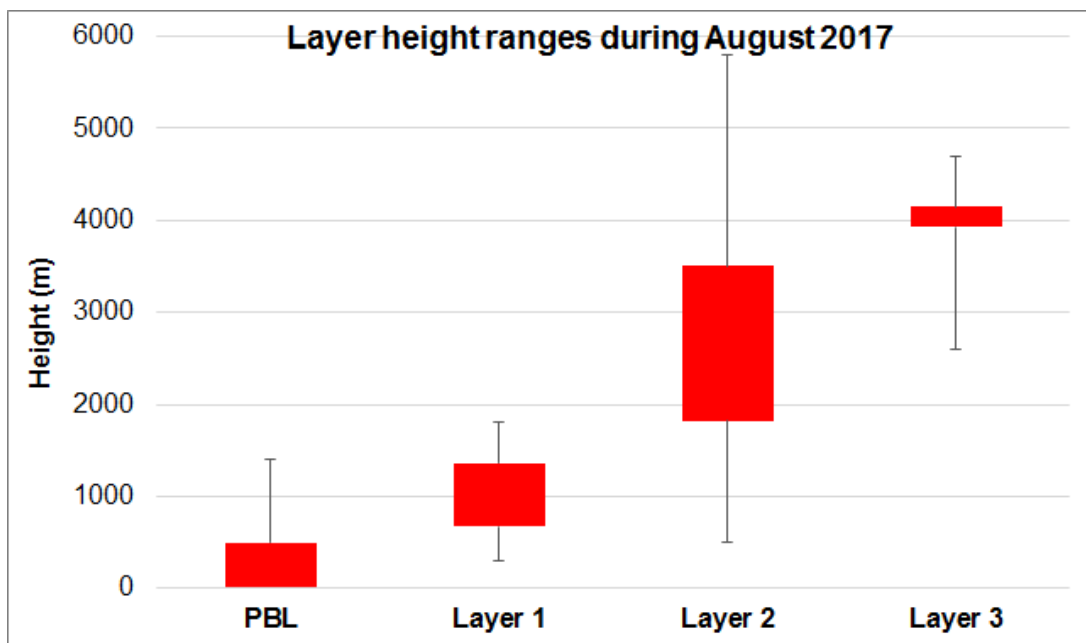
September 2017

Some of the aerosol layers of the 15 profiles from September 2017 reach heights up to 7000 m (Fig. 6.7a). SML is determined up to 2000 m and occurs in 30% of the cases below 1000 m, which is likely caused by the industrial and urban surrounds. Moreover, LAS is determined in 15% of all cases below 1000 m. The distribution of MIX ranges from the ground to 7000 m and it is the only type above 2000 m. The frequency of occurrence of MIX is larger compared to the other types: it is in over 30% of all cases up to 4500 m. One possible reason are the weather conditions. During September, the atmosphere above the eastern Mediterranean area was influenced by weak pressure gradients (low and high pressure systems at 500 hPa).

Considering Fig. 6.7 (b), the red boxes of PBL, Layer 1 and Layer 2 do not overlap each other. Only the outer 25% parts of Layers 1 and 2 show a large spread and so the occurrence of MIX up to 7000 m is based on Layer 2, because Layer 3 only covers a height range from 3500 to 4600 m. There are some few layers counted to the Layer 2 class which have a large vertical extension. In case of a Layer 3, the Layers 1 and 2 have a small vertical extensions.

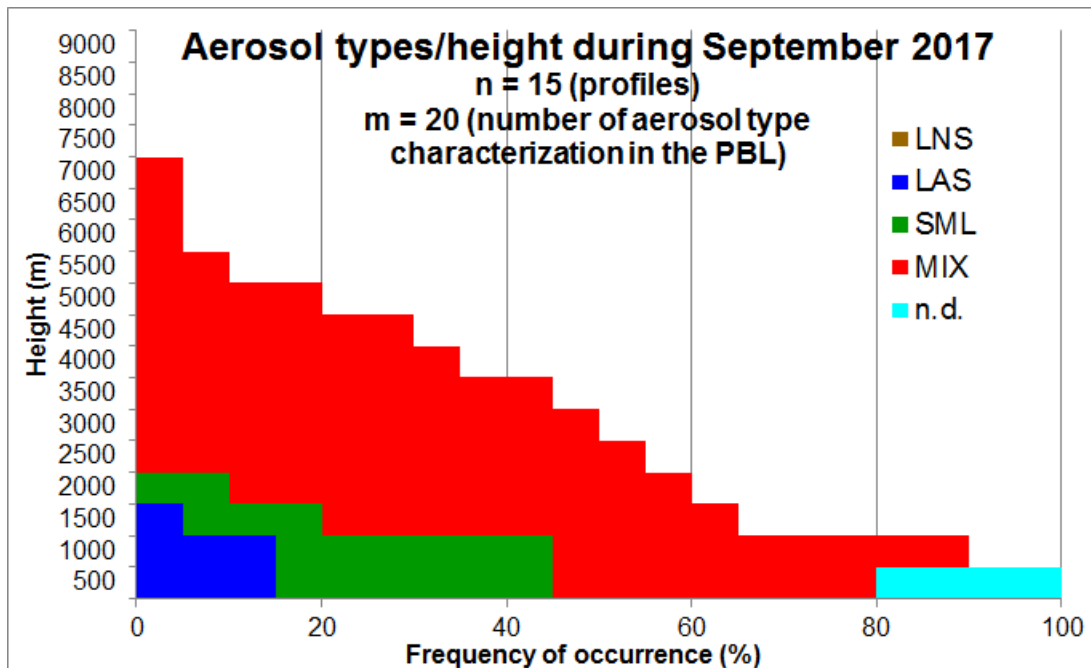


(a) Frequency of occurrence per interval of the aerosol types in August 2017. The height intervals are divided into 500 m bins. For example 500 m means every height between 1 and 500 m and 1000 m is 501 to 1000 m and so on.

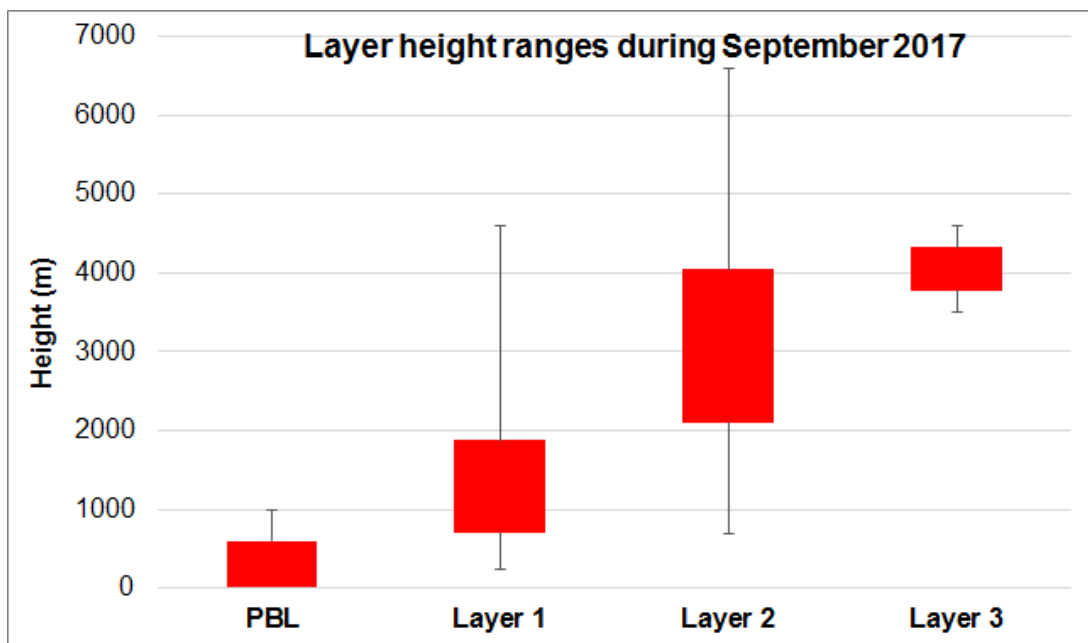


(b) Height ranges which are covered by the layers in August 2017 (PBL, Layer 1, Layer 2, Layer 3). The upper boundary of the red box marks 75% of the data and the lower boundary shows 25% of the data.

Figure 6.6: Aerosol types per interval and layer height ranges for August 2017.



(a) Frequency of occurrence per interval of the aerosol types in September 2017. The height intervals are divided into 500 m bins. For example 500 m means every height between 1 and 500 m and 1000 m is 501 to 1000 m and so on.



(b) Height ranges which are covered by the layers in September 2017 (PBL, Layer 1, Layer 2, Layer 3). The upper boundary of the red box marks 75% of the data and the lower boundary shows 25% of the data.

Figure 6.7: Aerosol types per interval and layer height ranges for September 2017.

March - September 2017

The statistical evaluation of the months March to September comprises 107 profiles (Fig. 6.8a). Below 500 m, 136 layers with aerosol type characterization were observed. The most common aerosol type is MIX. It can be found in all heights and it is the only occurring type between 8000 and 9000 m. MIX reaches a maximum frequency of 46% at 1500 m height.

LNS occurs up to an height of 7500 m and its frequency of occurrence is similarly in all heights. Between 2500 and 4000 m, the highest values of 7 and 8% of are reached.

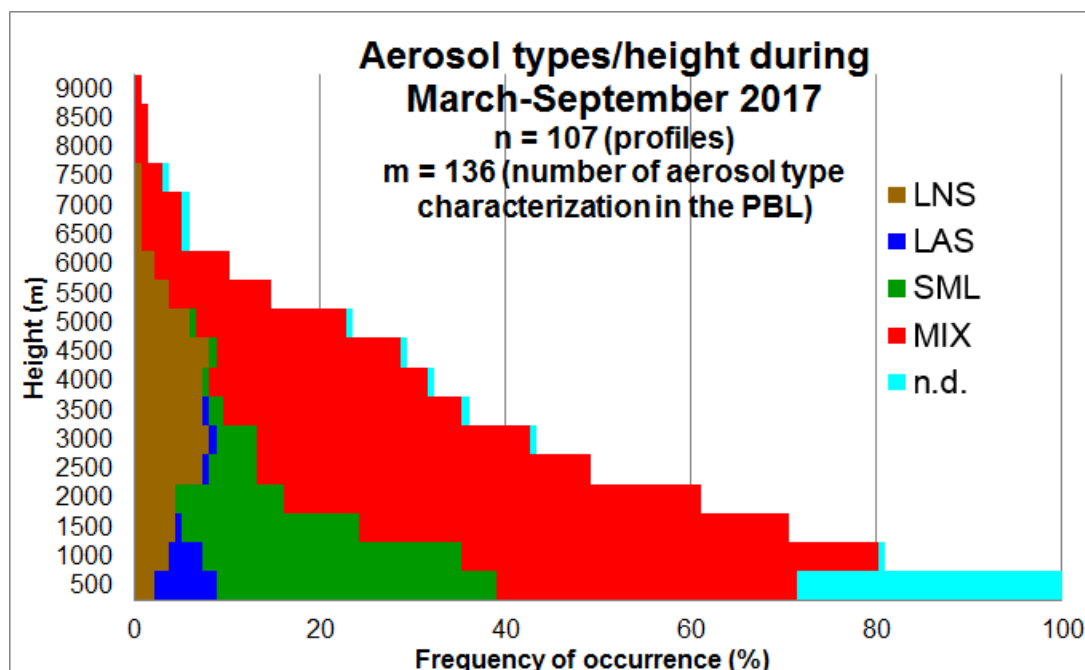
SML was determined up to 5000 m, but most of this aerosol type is distributed below 2500 m. It is obvious that small particles are rarely transported to larger heights and rather remain in the boundary layer. because of local sources.

The least occurring aerosol type is LAS which reached a height up to 3500 m. This aerosol type is mainly abundant in the lowest layer of the atmosphere. Due to the proximity to the Mediterranean Sea, these aerosol particles were not transported to larger heights and over longer distances.

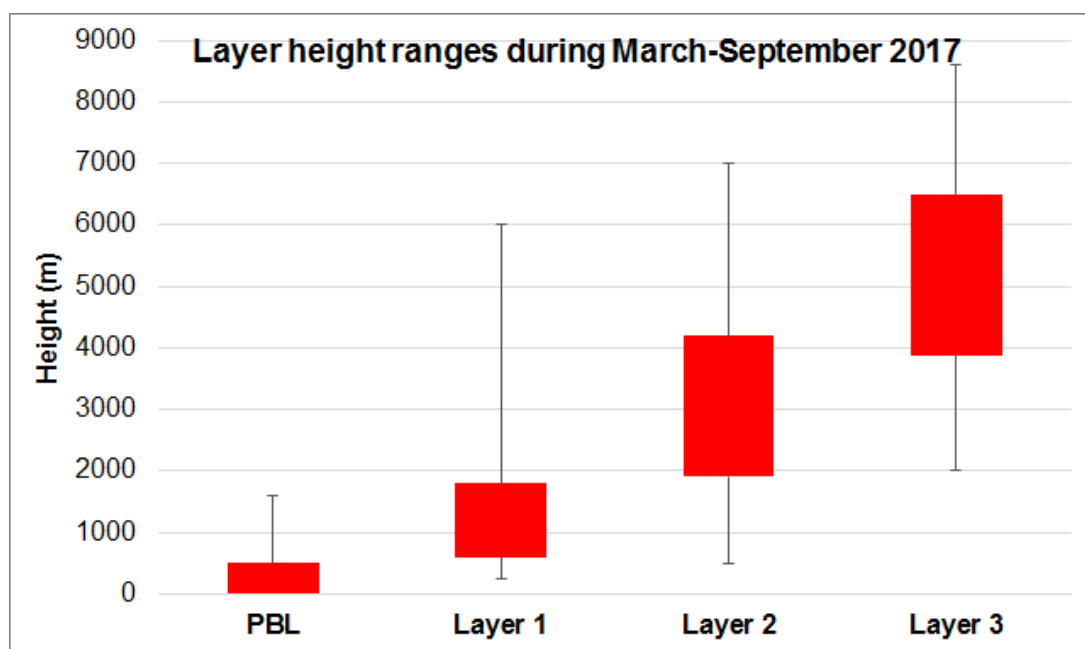
29% of all layers in the lowest height cannot be considered because of noise and overlap effects.

In Fig. 6.8 (b), the red boxes from PBL, Layer 1 and Layer 2 do not overlay each other. There is a weak overlap of Layer 2 with Layer 3 at around 4000 m. The spread of Layer 1, Layer 2 and Layer 3 shows that no general heights can be derived for the aerosol layers from the statistics. The individual layers either cover a vertically large height range or they are very thin and they are detected at different heights. This explains the large spread and some outliers of the individual layers.

The Polly^{XT} is continuously measuring at Haifa after September 2017, so further lidar data will be evaluated for other months. A seasonal variation in the individual aerosol types is expected to be observed from a full year data set, evaluated in ongoing work.



(a) Frequency of occurrence per interval of the aerosol types in the months March to September 2017. The height intervals are divided into 500 m bins. For example 500 m means every height between 1 and 500 m and 1000 m is 501 to 1000 m and so on.



(b) Height ranges which are covered by the layers in the months March to September 2017 (PBL, Layer 1, Layer 2, Layer 3). The upper boundary of the red box marks 75% of the data and the lower boundary shows 25% of the data.

Figure 6.8: Aerosol types per interval and layer height ranges for the months March to September 2017.

In conclusion, the influence of the Sharav cyclone is visible in the aerosol distribution because a larger dust content was determined until and including May. In general, more mix of dust with other aerosols than dust was observed. Most of the detected aerosol layers have a particle depolarization ratio between 0.07 and 0.2 and this large range might not be appropriate for the characterization of the aerosol layers above Haifa. But it is obvious that aerosol layers which have a particle depolarization ratio below and near 0.2 contain of more dust than aerosol layers with a particle depolarization ratio of 0.07. Therefore, values below 0.1 characterize less to non dust in those layers.

One example to check, if a mixed layer consists of small particles and large non-spherical particles, is the fine and coarse mode AOD retrievals of the AERONET sunphotometer measurements. For instance, the particle depolarization ratio (532 nm) of the aerosol layer between 500 and 1900 m at 8 July 2017 was 0.135. To exclude the mixture LNS and LAS, which is also possible with the linear particle depolarization ratio, this retrieval can be considered (available at the AERONET website for the site Technion Haifa). The fine and coarse mode fraction of the total measured AOD are equal during this day. So this might a further possible method to separate the mixtures.

7 Summary and discussion

This master thesis examine the vertical aerosol distribution at Haifa in Israel between March and September 2017. For this purpose, three case studies were presented and the aerosol types were characterized for the months March to September 2017.

The first case study deals with the development of the planetary boundary layer as it is detected by a lidar. The different parts of PBL according Stull (1988), e.g., mixed layer and residual layer, were determined by use of the 24-hours measurement from 4 April 2017. The mixed layer was detected from 7 UTC to sunset (16 UTC) and a residual layer with a maximum height of around 2500 m was observed near the sunset. In conclusion, the lidar is a tool to investigate the PBL in detail.

The investigation of the second case study about the land sea breeze on 27 May 2017 is based on the wind leap from 50 to 225 degrees and a low wind velocity. The measured quantities were compared to answer the question whether or not they change with the wind direction leap. Before the wind leap, a layer was detected between 2.6 and 3.6 km and after this wind leap, the atmosphere was well mixed. It was shown that the detection of land sea breeze with lidar at the measurement location at Haifa is very difficult due to overlap effects, since it is hard to capture a significant difference in the measured quantities in the lowest heights of this very small scale circulation because of the complex orographic conditions.

The third case study presents the dust event on 9 June 2017. A dust layer was detected in heights between 1000 and 3000 m and stayed homogeneous during the entire measuring period. The optical properties were constant with height within this layer. Vertical profiles of the intensive and extensive quantities were presented. The described aerosol characterization yielded to large non-spherical aerosol including mineral dust. Hence, the aerosol in this layer was identified as Saharan dust due to the characteristic values of the optical properties as well as backward trajectories. The conversion of the vertical profile into the mass concentration shows that this layer contains dust with a maximum quantity of $75 \mu\text{gm}^{-3}$ between 1500 and 3500 m. Further investigations of the transport with HYSPLIT and FLEXPART show that this layer was transported to Haifa from sources in north-eastern Africa. The transport was characterized by a low pressure system over

the Mediterranean Sea north of Libya and south of Greece and this low pressure system moved north-eastwards to Turkey.

The main part of the thesis deals with the aerosol type characterization (Baars et al., 2017). This characterization was applied to 107 manually evaluated lidar profiles of the measuring period from March to September 2017. The observed layers were analyzed regarding the aerosol type. Histograms of the aerosol types per height interval per month show the frequency of occurrence of the four investigated aerosol types: small (SML), mixed (MIX), large, spherical (LAS) and large, non-spherical (LNS).

It was shown that SML and MIX are distributed equally in the lowest height for March 2017. Although, LAS and LNS occurred in the upper heights. Often, MIX is observed. The aerosol distribution during April 2017 was mainly determined by LNS and MIX. MIX could be found in all heights up to 7000 m and LNS up to 5500 m. May was the only month where aerosol appeared up to 9000 m as mixed type. SML was detected below 2000 m and LNS in all heights up to 7500 m with a maximum frequency of 17% between 2500 and 4000 m. In June, the major part of the aerosol distribution contained SML and secondly of MIX. SML had a maximum frequency of 58% below 1000 m and reached up to 4000 m. The maximum of MIX was 29% between 2000 and 2500 m. The profiles of July were characterized by a frequent occurrence of MIX. This type can be found up to 7000 m with the highest frequency of 82% at 1000 m and it showed a frequency of occurrence to be greater than 50% below 4000 m. In August, MIX and SML dominate the distribution. In this case, the frequency of occurrence of SML was highest in the lowest layers and SML did not appear above 5000 m. In September, MIX was the most frequently occurring type and it is the only type between 2000 to 7000 m. SML reached up to 2000 m with values of the frequency of occurrence of 30% below 1000 m and LAS occurred in 15% of all cases below 1000 m. In total, the most frequently occurring aerosol type was the mixed type. A frequency of occurrence of LNS, which is the second most abundant type, was observed in all heights. SML could be found as the third-leading type and occurs mainly in the lowest layers. The least frequent type is LAS which appears only in the lowest heights.

The subtropical high caused stable weather conditions from June to August. Thus, the detected atmospheric particles had not been transported over long distances, but originated from the surrounds of Haifa. Urban (small) and industrial aerosol was detected and this has mixed with mineral dust from the surrounds of Haifa. The Sharav cyclone or rather low pressure systems from the west mainly influenced the aerosol distribution in April and May. These conditions enable dust to be transported from the Saharan desert over long distances to Haifa where the dust particles mixed with other aerosol types.

In conclusion, the mixed type was frequently detected in Haifa. It is difficult to identify the individual parts of MIX and their respective mixing ratio with the used

method. Therefore, further possibilities are presented to distinguish the components of mixed aerosol.

As a first method, the Ångström exponent $\mathring{A}_{532-1064}$ can complement the criteria for the mixed type with conditions of the Ångström exponent for the small and the large, spherical aerosol type. For example, if a mixed type has a value less than 0.75 for $\mathring{A}_{532-1064}$, it will be dominated by large particles. The mixed type is dominated by smaller particles when $\mathring{A}_{532-1064}$ is greater than or equal to 0.75.

A method to identify the amount of dust is the POLIPHON method like it has already been applied for the case study in Sect. 5.3. The method would make sense because of the closeness to desert regions. But these calculations could not be applied to all 107 profiles since they are still not run automatically. Another way is to use the fine and coarse mode AOD retrievals of the AERONET sunphotometer measurements. By those, it might be determinable, if the mixture consists of small and large particles (SML and LAS or SML and LNS) or only large particles (LAS and LNS).

A further possibility is the lidar ratio which could be used to extend the presented aerosol typing. The values of the lidar ratio for the respective layers are available for the measuring period (Table 6.1). The lidar ratio of a mixture of dust with marine aerosol is smaller than a mixture of dust with urban aerosol. Mixture formulas, developed by Groß et al. (2011b), can be applied to calculate the particle depolarization ratio and lidar ratio of a mixture theoretically from the particle depolarization ratio and lidar ratio from pure aerosol types. Groß et al. (2013) calculate particle depolarization ratio and the lidar ratio for different amounts of Saharan dust. The lidar ratio was contrasted with the linear particle depolarization ratio. Therefore, the lidar ratio and the linear particle depolarization ratio are calculated for a mixture of Saharan dust with Canadian biomass burning aerosol and Saharan dust with marine aerosol. Based on this, some mixing lines can be worked where the outer lines characterize the minimum and the maximum range of the input values and the central line defines the mean values of this calculation for the different mixtures. On the basis of mixing lines, it is possible to determine the detected mixture with the measured lidar ratio and linear particle depolarization ratio.

Burton et al. (2012) contrast the backscatter color ratio (ratio of backscatter coefficient at 532 to 1064 nm) with the lidar ratio (532 nm). Marine aerosol has values between 15 to 35 sr for the lidar ratio and 1.3 to 1.6 for the backscatter color ratio. The values for urban aerosol are 50 to 70 sr for the lidar ratio and 1.5 and 2.0 for the backscatter color ratio. The lidar ratio is determined 40 to 50 sr for pure dust and the backscatter ratio has values between 1.3 and 1.7. So this might be a possibility to estimate the different aerosol types of the detected mixture in the aerosol layer.

List of Tables

2.1	Products of the lidar Polly ^{XT} and their relative uncertainties based on Hofer et al. (2017).	17
3.1	Aerosol type criteria based on the measured linear particle depolarization ratio and Ångström exponent (Baars et al., 2017).	22
6.1	Manually recorded quantities for each aerosol layer.	38

List of Figures

2.1	(a) Polly ^{XT} on the roof of Technion in Haifa; (b) Open system showing major parts of Polly ^{XT} : sensors for outdoor temperature and rain (1), roof cover (2), air conditioner (3), laser head and optical system (4), receiver with 8 channels (5), drawer with 4 sensors for the near-range channels (6), laser power supply (7); based on Althausen et al. (2009) and Engelmann et al. (2016).	18
4.1	Vertical scheme of the PBL over land in high pressure regions. PBL consists of a very turbulent mixed layer, a less-turbulent residual layer and a nocturnal stable boundary layer. The mixed layer can be divided into a cloud layer and a subcloud layer (Stull, 1988).	24
4.2	Monthly distribution of the average accumulated dust (columns) and number of observations (line) at the site Beer Sheba (a). The dust distribution among the synoptic systems is demonstrated by the number of dust observations and the accumulated dust (b). The measurements were taken from 1967 to 2003 (Dayan et al., 2007).	27
4.3	Illustration showing the land sea breeze during day and night (Forkel, 2015).	28
5.1	Uncalibrated attenuated backscatter coefficient (1064 nm) from 04.04.2017 with marked time of sunrise (06:23 LT, 03:23 UTC), noon (12:42 LT, 09:42 UTC), sunset (19:02 LT, 16:02 UTC) and midnight as well as determined heights of PBL (brown lines).	30
5.2	Measurement of wind velocity (blue line) and wind direction (red line) at Haifa University (https://ims.data.gov.il/) on 27 May 2017. The two green boxes mark the lidar measurement before (07:23-08:21 UTC, 10:23-11:21 LT) and after (14:00-15:00 UTC, 17:00-18:00 LT) the wind leap.	31
5.3	Uncalibrated attenuated backscatter coefficient (1064 nm) on 27 May 2017 with investigation period from 07:23-08:21 UTC (before the wind leap, black box) and from 14:00-15:00 UTC (after the wind leap, red box).	32

5.4	Vertical profiles of particle backscatter coefficient (532 nm), Ångström exponent (355/532 nm) and particle depolarization ratio (532 nm) for 27 May 2017 07:23-08:21 UTC (before the wind leap, blue line) and 14:00-15:00 UTC (after the wind leap, green line). The error bar calculation is based on Hofer et al. (2017).	32
5.5	Uncalibrated attenuated backscatter coefficient (1064 nm) on 9 June 2017 with red box from 16:45-17:58 UTC indicating the averaging time of the profiles in Fig. 5.6.	33
5.6	Vertical profiles of the particle backscatter coefficient, particle extinction coefficient, lidar ratio, linear depolarization ratio, Ångström exponent and mass concentration for the respective wavelengths on 9 June 2017 16:45-17:58 UTC. The error bar calculations are based on Hofer et al. (2017). . .	34
5.7	NOAA HYSPLIT model backward trajectories for Haifa (32.78 N, 35.03 E) at 9 June 2017 17 UTC. Three heights have been calculated (1300, 2000, 2800 m AGL) for a duration of 114 hours.	35
5.8	Model calculation FLEXPART for 9 June 2017 for the height range from 1300 to 2700 m. The computation was done for 4 days backwards. The color bar scale is the logarithm of the accumulated residence time below 3 km of trajectories ending in Haifa.	36
5.9	Isohypsis 700 hPa geopotential (≈ 3000 m) with spacing of 5 hPa. Colors represent the wind speed at 700 hPa (blue ≈ 2 ms ⁻¹ , green ≈ 7 ms ⁻¹ , yellow ≈ 10 ms ⁻¹ , orange ≈ 16 ms ⁻¹ , red ≈ 22 ms ⁻¹). This GFS model output from NOAA (National Oceanic and Atmospheric Administration) is visualized with the program "zyGrib" (www.zygrib.org).	36
6.1	Aerosol types per interval and layer height ranges for March 2017.	40
6.2	Aerosol types per interval and layer height ranges for April 2017.	41
6.3	Aerosol types per interval and layer height ranges for May 2017.	44
6.4	Aerosol types per interval and layer height ranges for June 2017.	45
6.5	Aerosol types per interval and layer height ranges for July 2017.	46
6.6	Aerosol types per interval and layer height ranges for August 2017.	48
6.7	Aerosol types per interval and layer height ranges for September 2017.	49
6.8	Aerosol types per interval and layer height ranges for the months March to September 2017.	51

List of abbreviations

AERONET	Aerosol Robotic Network
AOD	Aerosol optical depth
EARLINET	European Aerosol Research Lidar Network
EZ	Entrainment zone
FLEXPART	Flexible Particle dispersion model
GFS	Global Forecast System
HYSPLIT	Hybrid Single-Particle Lagrangian Integrated Trajectory model
LAS	Large, spherical aerosol (aerosol classification)
Lidar	Light detection and ranging
LNS	Large, non-spherical aerosol (aerosol classification)
MIX	Aerosol-mix, partly non-spherical (aerosol classification)
ML	Mixed layer
NBL	Nocturnal boundary layer
n.d.	Not definable (aerosol classification)
NOAA	National Oceanic Atmospheric Administration
PBL	Planetary boundary layer
Poliphon	Polarization-lidar photometer networking
Polly^{XT}	Portable multi-wavelength Raman and polarization lidar system with eXTended capabilities
RL	Residual layer
SBL	Stable boundary layer
SL	Surface layer
SML	Small aerosol (aerosol classification)

Literature

- Althausen, D., Engelmann, R., Baars, H., Heese, B., Ansmann, A., Müller, D., and Kompula, M. (2009). Portable Raman lidar PollyXT for automated profiling of aerosol backscatter, extinction, and depolarization. *Journal of Atmospheric and Oceanic Technology*, 26(11):2366–2378. doi:10.1175/2009JTECHA1304.1.
- Ångström, K. (1906). Papers Communicated to the Second Conference, held at Oxford, September, 1905. No. 23. On the methods for the investigation of the Changes in Solar Radiation. *Transactions of the International Union for Cooperation in Solar Research*, 1:180–184.
- Ansmann, A., Riebesell, M., Wandinger, U., Weitkamp, C., and Michaelis, W. (1992a). Independent measurement of extinction and backscatter profiles in cirrus clouds by using a combined Raman elastic-backscatter lidar. *Applied Optics*, 31(33):7113–7131.
- Ansmann, A., Riebesell, M., Wandinger, U., Weitkamp, C., Voss, E., Lahmann, W., and Michaelis, W. (1992b). Combined raman elastic-backscatter lidar for vertical profiling of moisture, aerosol extinction, backscatter, and lidar ratio. *Applied Physics B: Photophysics and Laser Chemistry*, 55(1):18–28.
- Ansmann, A., Seifert, P., Tesche, M., and Wandinger, U. (2012). Profiling of fine and coarse particle mass: case studies of Saharan dust and Eyjafjallajökull/Grimsvötn volcanic plumes. *Atmospheric Chemistry and Physics*, 12(20):9399–9415. doi:10.5194/acp-12-9399-2012.
- Ansmann, A., Tesche, M., Seifert, P., Groß, S., Freudenthaler, V., Apituley, A., Wilson, K.M., Serikov, I., Linné, H., Heinold, B., et al. (2011). Ash and fine-mode particle mass profiles from EARLINET-AERONET observations over central Europe after the eruptions of the Eyjafjallajökull volcano in 2010. *Journal of Geophysical Research*, 116(D00U02). doi:10.1029/2010JD015567.
- Baars, H., Ansmann, A., Engelmann, R., and Althausen, D. (2008). Continuous mon-

- itoring of the boundary-layer top with lidar. *Atmospheric Chemistry and Physics*, 8(23):7281–7296. <http://www.atmos-chem-phys.net/8/7281/2008/>.
- Baars, H., Kanitz, T., Engelmann, R., Althausen, D., Heese, B., Komppula, M., Preifler, J., Tesche, M., Ansmann, A., Wandinger, U., et al. (2016). An overview of the first decade of PollyNET: an emerging network of automated Raman-polarization lidars for continuous aerosol profiling. *Atmospheric Chemistry and Physics*, 16(8):5111–5137. doi:10.5194/acp-16-5111-2016.
- Baars, H., Seifert, P., Engelmann, R., and Wandinger, U. (2017). Target categorization of aerosol and clouds by continuous multiwavelength-polarization lidar measurements. *Atmospheric Measurement Techniques*, 10(9):3175–3201. <http://doi.org/10.5194/amt-10-3175-2017>.
- Bohren, C. F. and Huffman, D. R., editors (1983). *Absorption and Scattering of Light by Small Particles*. John Wiley & Sons, Inc. New York, NY.
- Burton, S. P., Ferrare, R.A., Hostetler, C.A., Hair, J.W., Rogers, R.R., Obland, M.D., Butler, C.F., Cook, A.L., Harper, D.B., and Froyd, K.D. (2012). Aerosol classification using airborne High Spectral Resolution Lidar measurements - methodology and examples. *Atmospheric Measurement Techniques*, 5(1):73–98. doi:10.5194/amt-5-73-2012.
- Charlson, R. J. and Heintzenberg, J. (1995). *Aerosol forcing of climate*, volume 11. John Wiley & Sons New York, NY. Dahlem Workshop on Aerosol Forcing of Climate.
- Dai, G., Althausen, D., Hofer, J., Engelmann, R., Seifert, P., Bühl, J., Mamouri, R.-E., Wu, S., and Ansmann, A. (2018). Calibration of Raman lidar water vapor profiles by means of AERONET photometer observations and GDAS meteorological data. *Atmospheric Measurement Techniques*, 11(5):2735–2748. <http://doi.org/10.5194/amt-11-2735-2018>.
- Dayan, U. and Rodnizki, J. (1999). The temporal behavior of the atmospheric boundary layer in Israel. *Journal of Applied Meteorology*, 38(6):830–836.
- Dayan, U., Ziv, B., Shoob, T., and Enzel, Y. (2007). Suspended dust over southeastern Mediterranean and its relation to atmospheric circulations. *International Journal of Climatology*, 28(7):915–924. doi:10.1002/joc.1587.
- Demtröder, W. (2009). *Experimentalphysik 2 - Elektrizität und Optik*. Springer-Verlag Berlin, Heidelberg, 5th edition.

- Engelmann, R., Kanitz, T., Baars, H., Heese, B., Althausen, D., Skupin, A., Wandinger, U., Komppula, M., Stachlewska, I.S., and Amiridis, V. (2016). The automated multi-wavelength Raman polarization and water-vapor lidar PollyXT: the neXT generation. *Atmospheric Measurement Techniques*, 9:1767–1784. doi:10.5194/amt-9-1767-2016.
- Fernald, F. G. (1984). Analysis of atmospheric lidar observations: some comments. *Applied Optics*, 23(5):652–653.
- Flexpart (2018). Official FLEXPART web site. online available <http://www.flexpart.eu/>; retrieved 09.02.2018.
- Forkel, M. (2015). Land-See-Windssystem. online available <http://www.klima-der-erde.de/winde.html#land-see>; retrieved 21.12.2017.
- Freudenthaler, V., Esselborn, M., Wiegner, M., Heese, B., Tesche, M., Ansmann, A., Müller, D., Althausen, D., Wirth, M., Fix, A., et al. (2009). Depolarization ratio profiling at several wavelengths in pure Saharan dust during SAMUM 2006. *Tellus B: Chemical and Physical Meteorology*, 61B(1):165–179. doi:10.1111/j.1600-0889.2008.00396.x.
- Ganor, E., Levin, Z., and Van Grieken, R. (1998). Composition of individual aerosol particles above the Israelian Mediterranean coast during the summer time. *Atmospheric Environment*, 32(9):1631–1642.
- Giannakaki, E., Balis, D.S., Amiridis, V., and Zerefos, C. (2010). Optical properties of different aerosol types: seven years of combined Raman-elastic backscatter lidar measurements in Thessaloniki, Greece. *Atmospheric Measurement Techniques*, 3(3):569–578. doi:10.5194/amt-3-569-2010.
- Groß, S., Esselborn, M., Weinzierl, B., Wirth, M., Fix, A., and Petzold, A. (2013). Aerosol classification by airborne high spectral resolution lidar observations. *Atmospheric Chemistry and Physics*, 13(5):2487–2505. doi:10.5194/acp-13-2487-2013.
- Groß, S., Gasteiger, J., Freudenthaler, V., Wiegner, M., Geiß, A., Schladitz, A., Toledano, C., Kandler, K., Tesche, M., Ansmann, A., and Wiedensohler, A. (2011a). Characterization of the planetary boundary layer during SAMUM-2 by means of lidar measurements. *Tellus B: Chemical and Physical Meteorology*, 63(4):695–705. doi:10.1111/j.1600-0889.2011.00557.x.
- Groß, S., Tesche, M., Freudenthaler, V., Toledano, C., Wiegner, M., Ansmann, A., Althausen, D., and Seefeldner, M. (2011b). Characterization of Saharan dust,

- marine aerosols and mixtures of biomass-burning aerosols and dust by means of multi-wavelength depolarization and Raman lidar measurements during SAMUM 2. *Tellus B: Chemical and Physical Meteorology*, 63(4):706–724. doi:10.1111/j.1600-0889.2011.00556.x.
- Groß, S. M. (2011). *Aerosol characterization by multi-wavelength Raman- and depolarization lidar observations*. PhD thesis, LMU Munich.
- Haarig, M., Ansmann, A., Gasteiger, J., Kandler, K., Althausen, D., Baars, H., Radenz, M., and Farrell, D. A. (2017). Dry versus wet marine particle optical properties: RH dependence of depolarization ratio, backscatter, and extinction from multiwavelength lidar measurements during SALTRACE. *Atmospheric Chemistry and Physics*, 17(23):14199–14217. <http://doi.org/10.5194/acp-17-14199-2017>.
- Hallquist, M., Wenger, J.C., Baltensperger, U., Rudich, Y., Simpson, D., Claeys, M., Dommen, J., Donahue, N.M., George, C., Goldstein, A.H., et al. (2009). The formation, properties and impact of secondary organic aerosol: current and emerging issues. *Atmospheric Chemistry and Physics*, 9(14):5155–5236. <http://www.atmos-chem-phys.net/9/5155/2009/>.
- Hofer, J., Althausen, D., Abdullaev, S. F., Makhmudov, A. N., Nazarov, B. I., Schettler, G., Engelmann, R., Baars, H., Fomba, K. W., Müller, K., et al. (2017). Long-term profiling of mineral dust and pollution aerosol with multiwavelength polarization Raman lidar at the Central Asian site of Dushanbe, Tajikistan: case studies. *Atmospheric Chemistry and Physics*, 17(23):14559–14577. <http://doi.org/10.5194/acp-17-14559-2017>.
- Holben, B. N., Eck, T.F., Slutsker, I., Tanré, D., Buis, J.P., Setzer, A., Vermote, E., Reagan, J.A., Kaufman, Y.J., Nakajima, T., et al. (1998). AERONET—A Federated Instrument Network and Data Archive for Aerosol Characterization. *Remote Sensing of Environment*, 66(1):1–16.
- Holben, B. N., Tanré, D., Smirnov, A., Eck, T.F., Slutsker, I., Abuhassan, N., Newcomb, W.W., Schafer, J.S., Chatenet, B., Lavenu, F., et al. (2001). An emerging ground-based aerosol climatology: Aerosol optical depth from AERONET. *Journal of Geophysical Research*, 106(D11):12067–12097. doi:2001JD900014.
- Israelevich, P. L., Ganor, E., Levin, Z., and Joseph, J. H. (2003). Annual variations of physical properties of desert dust over Israel. *Journal of Geophysical Research*, 108(D13). doi:10.1029/2002JD003163.

- Klein, V. and Werner, C. (1993). *Fernmessung von Luftverunreinigungen: mit Lasern und anderen spektroskopischen Verfahren*. Springer Verlag Berlin, Heidelberg.
- Klett, J. D. (1981). Stable analytical inversion solution for processing Lidar returns. *Applied Optics*, 20(2):211–220.
- Koçak, M., Nimmo, M., Kubilay, N., and Herut, B. (2004). Spatio-temporal aerosol trace metal concentrations and sources in the Levantine Basin of the Eastern Mediterranean. *Atmospheric Environment*, 38(14):2133–2144. doi:10.1016/j.atmosenv.2004.01.020.
- Kubilay, N., Nickovic, S., Moulin, C., and Dulac, F. (2000). An illustration of the transport and deposition of mineral dust onto the eastern Mediterranean. *Atmospheric Environment*, 34(8):1293–1303.
- Mamouri, R.-E. and Ansmann, A. (2014). Fine and coarse dust separation with polarization lidar. *Atmospheric Measurement Techniques*, 7(11):3717–3735. doi:10.5194/amt-7-3717-2014.
- Mamouri, R.-E., Ansmann, A., Nisantzi, A., Kokkalis, P., Schwarz, A., and Hadjimitsis, D. (2013). Low Arabian dust extinction-to-backscatter ratio. *Geophysical Research Letters*, 40(17):4762–4766. doi:10.1002/grl.50898.
- Michael, T., Kammler, W., Möhle, A., Richter, B., and Schlimm, R., editors (2002). *Diercke Weltatlas*. Westermann Schulbuchverlag GmbH, Braunschweig, 5th edition.
- Mie, G. (1908). Beiträge zur Optik trüber Medien, speziell kolloidaler Metallösungen. *Annalen der Physik*, 25(4):377–445.
- Müller, D., Mattis, I., Wandinger, U., Ansmann, A., Althausen, D., Dubovik, O., Eckhardt, S., and Stohl, A. (2003). Saharan dust over a central European EARLINET-AERONET site: Combined observations with Raman lidar and Sun photometer. *Journal of Geophysical Research*, 108(D12). doi:10.1029/2002JD002918.
- Nisantzi, A., Mamouri, R.-E., Ansmann, A., Schuster, G.L., and Hadjimitsis, D.G. (2015). Middle East versus Saharan dust extinction-to-backscatter ratios. *Atmospheric Chemistry and Physics*, 15(12):7071–7084. doi:10.5194/acp-15-7071-2015.
- Osetinsky, I. (2006). *Climate changes over the Eastern Mediterranean - A synoptic systems classification approach*. PhD thesis, Tel Aviv University.

- Pfeffer, G. (2017). Land-See-Wind. online available http://www.gerd-pfeffer.de/zirk_wind_landsee.html; retrieved 08.09.2017.
- Roedel, W. and Wagner, T. (2011). *Physik unserer Umwelt: Die Atmosphäre*. Springer-Verlag Berlin, Heidelberg, 4th edition.
- Rolph, G., Stein, A., and Stunder, B. (2017). Real-time Environmental Applications and Display sYstem: READY. *Environmental Modelling & Software*, 95:210–228. <http://dx.doi.org/10.1016/j.envsoft.2017.06.025/>.
- Sasano, Y., Browell, E. V., and Ismail, S. (1985). Error caused by using a constant extinction/backscattering ratio in the lidar solution. *Applied Optics*, 24(22):3929–3932.
- Seinfeld, J. H. and Pandis, S. N. (1998). *Atmospheric Chemistry and Physics - From Air Pollution to Climate Change*. John Wiley and Sons, Inc. New York, NY.
- Stein, A. F., Draxler, R.R., Rolph, G.D., Stunder, B.J.B., Cohen, M.D., and Ngan, F. (2015). NOAA’s HYSPLIT atmospheric transport and dispersion modeling system. *Bulletin of the American Meteorological Society*, 96(12):2059–2077. doi:10.1175/BAMS-D-14-00110.1.
- Stohl, A., Forster, C., Frank, A., Seibert, P., and Wotawa, G. (2005). The lagrangian particle dispersion model FLEXPART version 6.2. *Atmospheric Chemistry and Physics*, 5(9):2461–2474. <http://www.atmos-chem-phys.org/acp/5/2461/>.
- Stull, R. B. (1988). *An Introduction to Boundary Layer Meteorology*. Kluwer Academic Publishers, Dordrecht.
- Tesche, M., Ansmann, A., Müller, D., Althausen, D., Mattis, I., Heese, B., Freudenthaler, V., Wiegner, M., Esselborn, M., Pisani, G., et al. (2009). Vertical profiling of Saharan dust with Raman lidars and airborne HSRL in southern Morocco during SAMUM. *Tellus B: Chemical and Physical Meteorology*, 61B(1):144–164. doi:10.1111/j.1600-0889.2008.00390.x.
- WeatherUnderground-April (2018). Wetterverlauf für Flughafen Haifa (LLHA) - April, 2017. online available http://www.wunderground.com/history/airport/LLHA/2017/4/4/DailyHistory.html?req_city=&req_state=&req_statename=&reqdb.zip=&reqdb.magic=&reqdb.wmo=; retrieved 08.03.2018.
- Weitkamp, C., editor (2006). *Lidar: range-resolved optical remote sensing of the atmosphere*. Springer Science & Business Media Inc. New York, NY.

Selbstständigkeitserklärung

Hiermit erkläre ich, dass ich die vorliegende Masterarbeit selbstständig und nur unter Verwendung der angegebenen Literatur und Hilfsmittel angefertigt habe. Die aus fremden Quellen direkt oder indirekt übernommenen Stellen sind als solche kenntlich gemacht. Die Arbeit wurde bisher in gleicher oder ähnlicher Form keiner anderen Prüfungsbehörde vorgelegt und auch nicht veröffentlicht.

Ort, Datum

Unterschrift